DEVELOPMENTAL BIOLOGY

Activating transcription factor 3 coordinates differentiation of cardiac and hematopoietic progenitors by regulating glucose metabolism

Hui-Min Yin[1]*, Li-Feng Yan[1]*, Qian Liu[2], Zheng Peng[1], Chi-Yuan Zhang[1], Yu Xia[1], Dan Su[1], Ai-Hua Gu[2]†, Yong Zhou[1]†

The cardiac and hematopoietic progenitors (CPs and HPs, respectively) in the mesoderm ultimately form a well-organized circulation system, but mechanisms that reconcile their development remain elusive. We found that activating transcription factor 3 (*atf3*) was highly expressed in the CPs, HPs, and mesoderm, in zebrafish. The *atf3*$^{-/-}$ mutants exhibited atrial dilated cardiomyopathy and a high ratio of immature myeloid cells. These manifestations were primarily caused by the blockade of differentiation of both CPs and HPs within the anterior lateral plate mesoderm. Mechanistically, Atf3 targets *cebpγ* to repress *slc2a1a*-mediated glucose utilization. The high rate of glucose metabolism in *atf3*$^{-/-}$ mutants inhibited the differentiation of progenitors by changing the redox state. Therefore, *atf3* could provide CPs and HPs with metabolic adaptive capacity to changes in glucose levels. Our study provides new insights into the role of *atf3* in the coordination of differentiation of CPs and HPs by regulating glucose metabolism.

INTRODUCTION

The heart and blood are important components of the circulatory system. They are commonly derived from the mesoderm; they exhibit similar expression patterns of mesodermal regulatory genes, such as *FLK1*. The specified cardiac progenitors (CPs) are localized in the posterior region of the anterior lateral plate mesoderm (ALPM), adjacent to the hematopoietic progenitors (HPs), which reside in the rostral region (*1*). The development of cardiac and hematopoietic cell lineages is thus intimately connected in the cellular framework of the ALPM, suggesting coordinated development. Consistent with this notion, it has been reported that certain congenital heart defects are associated with hematopoietic disorders. For instance, cardiac abnormalities and leukemia are observed in Down syndrome (*2*), Digeorge syndrome (*3*), and Noonan and Leopard syndromes (*4*), and dilated cardiomyopathy and neutropenia are observed in Barth syndrome (*5*). Therefore, delineating mechanisms that coordinate the development of CPs and HPs may improve our understanding of those congenital heart diseases (CHDs).

Previous studies indicated antagonism between the developmental signaling pathways of CPs and HPs. During hematopoiesis, *Scl/Tal1* is mainly responsible for the activation of hemogenic competence in hemangioblasts. HPs in the ALPM give rise mostly to cells of the myeloid lineage in a *Scl/Tal1*-dependent manner, while loss of *Scl/Tal1* or its upstream regulator *Etv2* switches hematopoietic and endothelial lineages to cardiac lineages in mouse embryos (*6*, *7*). During cardiac development, *Nkx2.5* is broadly expressed in the CPs of both the first heart field (FHF) and the second heart field (SHF) and mediates myocardial differentiation (*8*). *Nkx2.5* can also prohibit hematopoietic development by repressing *Scl/Tal1* (*9*) and the erythroid master regulator *Gata1* (*10*). *Hand2*, a transcription factor expressed broadly in bilateral areas within the ALPM, promotes the formation of the FHF at the expense of hematopoietic and vascular lineages (*11*). Despite the above potential antagonism between cell lineages, how the differentiation of CPs and HPs is coordinated remains elusive.

In this study, we analyzed the transcriptomes of mouse embryonic heart cells, HPs, mesodermal cells, and ectodermal cells to explore the shared mechanisms between cardiac and hematopoietic development. We found that activating transcription factor 3 (*Atf3*) was highly expressed in all three cell types compared with the ectodermal cells. ATF3, a basic leucine zipper transcription factor, has long been recognized as a cellular adaptive response factor. It was reported that pancreatic-specific overexpression of *Atf3* in mouse embryos restrained endocrine precursors from differentiating into glucagon/insulin-producing cells (*12*). Cardiac-specific overexpression of *Atf3* in mouse embryos resulted in cardiac hypertrophy and premature death (*13*). *Atf3*-knockout mice exhibited airway hyperresponsiveness, pulmonary eosinophilia, and enhanced CD4$^+$ lymphocyte activity (*14*). However, little is known about the role of ATF3 in cardiogenesis and hematopoiesis.

The transparent zebrafish model allows for unparalleled visualization and genetic dissection of early embryos, which are difficult to study in mammals. Taking advantage of this model, we first confirmed that the zebrafish ortholog *atf3* transcripts were consistently enriched in *nkx2.5*$^+$ CPs on the basis of our previous microarray data (*15*). Then, we generated an *atf3*-knockout zebrafish line using the CRISPR-Cas9 system, and we found that *atf3*-deficient zebrafish developed a systemic circulation defect, including dilated cardiomyopathy and hematopoietic hyperplasia. We revealed that Atf3 primarily targeted the *cebpγ* gene, a key energy metabolic regulator, regulating glucose metabolism. Loss of *atf3* leads to a high rate of glucose utilization, and such metabolic change may cause the differentiation blockade of CPs and HPs. Collectively, our findings reveal

---

[1]CAS Key Laboratory of Tissue Microenvironment and Tumor, Shanghai Institute of Nutrition and Health, Shanghai Institutes for Biological Sciences, University of Chinese Academy of Sciences, Chinese Academy of Sciences, Shanghai 200032, China. [2]State Key Laboratory of Reproductive Medicine, Institute of Toxicology, School of Public Health, Nanjing Medical University, Nanjing 211166, China.
*These authors contributed equally to this work.
†Corresponding author. Email: aihuagu@njmu.edu.cn (A.-H.G.); zhouyong@sibs.ac.cn (Y.Z.)

a previously unidentified role of *atf3* in coordinating the differentiation of CPs and HPs in the mesoderm by regulating glucose metabolism.

RESULTS

Atf3 is highly expressed in the mesoderm, CPs, and HPs

We isolated mouse embryonic heart cells at E9.5 (embryonic day 9.5), $CD45^+CD144^+$ HPs at E11.5, and the mesoderm and ectoderm at E7.5 to perform a transcriptomic sequencing analysis (fig. S1A). The MA plots show the profiles of differentially expressed genes in the mesodermal cells, embryonic heart cells, and HPs in comparison with ectodermal cells (Fig. 1A). The number of genes with up-regulated expression in the embryonic heart cells or HPs is much higher than that in the mesoderm. The transcripts of 1079 genes were uniquely enriched in the mesodermal cells. Among those, genes with up-regulated expression in both the embryonic heart cells and HPs are shown in the upper right quadrant in the scatterplot (Fig. 1B). We found that the expression of Atf3 was equally enriched in the two populations. Hence, we hypothesized that *Atf3* is a shared developmental regulator of the heart and blood.

The zebrafish is a widely used model for developmental studies because of its easily accessible and transparent embryos. Taking advantage of the zebrafish model, we first confirmed that zebrafish *atf3*, which is located on chromosome 20, shows high similarity to its mammalian ortholog (fig. S1B). Genes flanking the zebrafish *atf3* locus are syntenic with those flanking the *ATF3* locus in human (fig. S1C). Zebrafish *atf3* encodes a protein of 202 amino acids, which shares 88.7% sequence similarity with human ATF3 (fig. S1D). Furthermore, the expression of *atf3* transcripts in *nkx2.5*$^+$ CPs was 28.6-fold higher than that in *nkx2.5*$^-$ cells at 30 hours post-fertilization (hpf) in our microarray data (Fig. 1C) (*15*), indicating its potential roles in cardiogenesis.

CPs in the FHF and HPs share the *atf3* expression pattern

Whole-mount in situ hybridization (WISH) showed that *atf3* transcripts were enriched in the *nkx2.5*-expressing region harboring CPs within the ALPM at 9 somites (ss), 3 hours before the onset of CP differentiation (Fig. 1, D and E). Double WISH indicated that the *atf3*-expressing domain not only was localized in the caudal portion of the *hand2*$^+$ heart-forming region (Fig. 1, F and G) but also partly overlapped with the *tal1*$^+$ hemogenic region harboring HPs at 9 ss (Fig. 1, H and I). We found that *atf3* was expressed in the linear heart tube derived from the FHF at 30 hpf, but not in the arterial pole of the heart tube, known as the SHF (Fig. 1J). Subsequently, *atf3* transcripts were continuously expressed in the heart tube and could be detected in the hematopoietic stem cell (HSC) generating region aorta-gonad-mesonephros (AGM) and caudal hematopoietic tissue (CHT) at 32 hpf (Fig. 1K). The specific expression pattern of *atf3* suggested its potential role in the development of CPs and HPs.

For lineage tracing of the *atf3*$^+$ CP population, the transgenic fish line *Tg(atf3:RFP2Acre)* was generated with a 6.3-kb *atf3* promoter driving TagRFP and Cre cassettes. The expression pattern of RFP in *atf3:RFP* transgenic fish confirmed the *atf3* WISH data. *atf3:RFP* was detectable in the heart, AGM, and CHT at 32 hpf (Fig. 1L). The *Tg(atf3:RFP2Acre);Tg(cmlc2:eGFP)* (a cardiomyocyte marker) double transgenic embryos showed that *atf3*$^+$ cardiomyocytes were mainly located in the FHF-derived ventricular part and the atrium at 60 hpf (Fig. 1M). The *atf3*$^+$ cells minimally contributed to endocardium development in the ventricle and atrium, but they gave rise to the endothelial cells in the outflow tract and pharyngeal arch arteries (PAAs), as revealed by the *Tg(atf3:RFP2Acre);Tg(fli1a:nGFP)* (an endothelial marker) double transgenic embryos at this stage (Fig. 1N and fig. S2). To evaluate the contribution of *atf3*$^+$ descendants to the SHF-derived cardiac cells, the *Tg(atf3:RFP2Acre)* fish were crossed with the *Tg(ltbp3:eGFP)* fish, which expressed enhanced green fluorescent protein (eGFP) in the SHF-derived cells. As shown in Fig. 1O, the *atf3*$^+$ cells showed no overlap with eGFP$^+$ SHF-derived cells at 60 hpf.

To further confirm the expression pattern of *atf3*, the *Tg(atf3:RFP2Acre)* line was crossed to the *Tg(ubiquitin:CSY)* line, which carried a unique Cre-responsive "color switching" cassette (AmCyan-Switch-ZsYellow, CSY) under control of the *ubiquitin* promoter (Fig. 1P). Without cre-mediated recombination, all the cells in the *Tg(ubiquitin:CSY)* line would be labeled with blue fluorescence from the AmCyan protein. In Cre-expressing cells, the *amcyan* gene is deleted and the ZsYellow gene is turned on to label cells with yellow fluorescence. Such color switching pattern revealed that *atf3*$^+$ descendants with yellow fluorescence in the *Tg(atf3:RFP2Acre);Tg(ubiquitin:CSY)* embryos were restricted within the proximal part of the ventricle and the atrium at 60 hpf, which was derived from the CPs in the FHF (Fig. 1P). Notably, *atf3*$^+$ descendants were also present in the circulating blood (Fig. 1, M, N, and P), suggesting that *atf3* may also participate in HP development. Collectively, these data demonstrated that *atf3* is mainly expressed in CPs from the FHF but not the SHF, and it is also expressed in HPs, suggesting that *atf3* may coordinately regulate the differentiation of both CPs and HPs.

Loss of *atf3* causes dilated atrial cardiomyopathy

Loss-of-function experiments were performed using *atf3* mutant zebrafish lines that were generated by the CRISRP-Cas9 system. We obtained the homozygous *atf3* mutant lines as shown in table S1. None of the homozygous *atf3* mutant zebrafish showed apparent defects in viability or life span. However, the *atf3* mutants were weaker than their siblings and had a gill defect. The mutant line *atf3*$^{m1/m1}$ had a one–base pair deletion that resulted in a frameshift mutation with a premature stop codon in exon 2, leading to a truncated protein of 56 amino acids and loss of function (Fig. 2A). The pathological sections of *atf3*$^{-/-}$ embryos exhibited an atrophic ventricle and a dilated atrium compared with the wild-type (WT) controls at 72 hpf (Fig. 2B). The mutant lines showed consistent pathological phenotypes.

Compared with the WT control, *atf3*$^{-/-}$;*Tg(cmlc2:dsred*^{nuc}*)* embryos exhibited a significant decrease of ventricular cardiomyocytes by 17.6% and a drastic increase of atrial cardiomyocytes by 61.9%, whereas the total number of cardiomyocytes in the mutants remained unchanged (Fig. 2, C and D). Similarly, the number of endocardial cells decreased by 17.0% in the ventricle and increased by 49.9% in the atrium in *atf3*$^{-/-}$;*Tg(fli1a:GFP*^{nuc}*)* embryos compared with the WT, leaving the total number unchanged (Fig. 2, E and F). Following the embryonic defects, the 1-year-old *atf3*$^{-/-}$ adult fish developed a heart with enlarged atrium and smaller ventricle, compared with the WT controls (Fig. 2G), suggesting cardiac dysfunction.

We next performed electrocardiography (ECG) and echocardiography in WT and *atf3*$^{-/-}$ adults to further evaluate cardiac function. Notably, the ECG revealed that the P wave amplitude had a

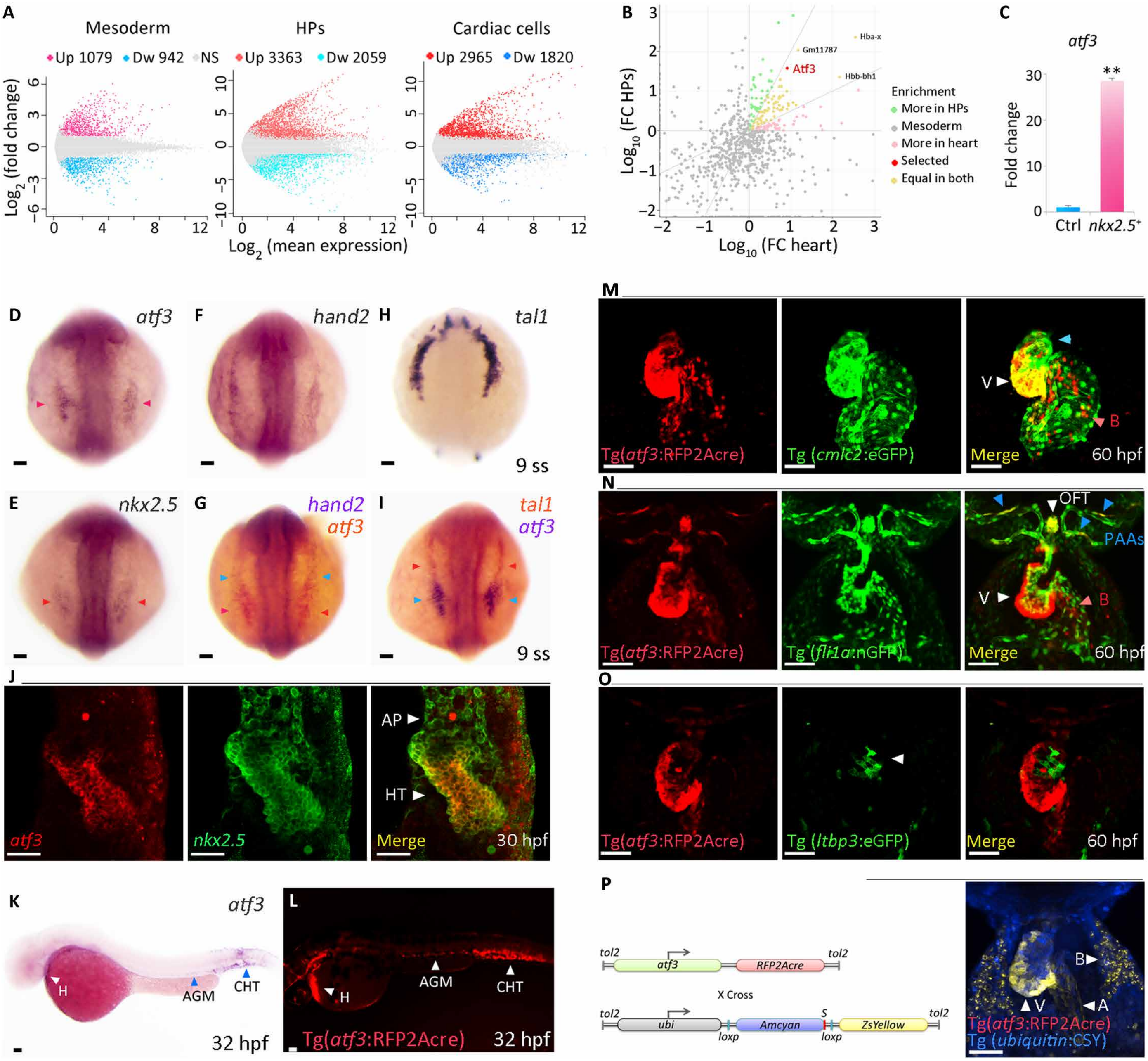

Fig. 1. The expression of *atf3* and the identification of the FHF. (**A**) MA plots showing the profiles of differentially expressed genes in the mesodermal cells at E7.5, in HPs at E11.5, and in embryonic cardiac cells at E9.5. Expression levels of genes in the ectoderm were used as control. The white line indicates the differentially expressed genes with twofold expression change. NS, no significance. (**B**) Genes with enriched expression in mesodermal cells [fold change (FC) ≥2]. Up-regulated genes with expression enrichment in both embryonic cardiac cells and HPs compared with mesodermal cells are highlighted as colored dots (green, yellow, and pink) in the upper right quadrant. Genes labeled by yellow dots were equally enriched in the blood and heart lineages. (**C**) mRNA expression level of *atf3* in *nkx2.5*$^+$ CPs based on microarray data in zebrafish at 30 hpf. Statistical analysis was carried out using the unpaired two-tailed Student's *t* test. Error bars indicate SD, $^{**}P < 0.01$ ($n = 3$ per group). (**D** and **E**) WISH of *atf3* and *nkx2.5* at 9 ss. Red arrowheads indicate that the expression position of *atf3* was comparable with that of *nkx2.5*. (**F**) WISH of *hand2* at 9 ss. (**G**) Colocalization analysis of mRNA expression patterns of *hand2* (blue arrowheads) and *atf3* (red arrowheads). (**H**) WISH of *tal1* at 9 ss. (**I**) Colocalization analysis of mRNA expression patterns of *tal1* (red arrowheads) and *atf3* (blue arrowheads). (**J**) Fluorescent in situ hybridization of *atf3* combined with immunofluorescence staining of Nkx2.5 at 30 hpf. AP, arterial pole; HT, heart tube. (**K**) Expression enrichment of *atf3* in the heart tube (H, white arrowhead), AGM, and CHT (blue arrowheads) at 32 hpf. (**L**) Fluorescent expression of *atf3*:*RFP2ACre* stable line at 32 hpf. (**M** and **N**) Colocalization analysis of (M) Atf3 and Cmlc2 and (N) Atf3 and Fli1a using transgenic lines at 60 hpf. V, ventricle; OFT, outflow tract; B, blood. (**O**) Complementary expression of RFP and eGFP fluorescence in the ventricle in *Tg(atf3:RFP2Acre); Tg(ltbp3:eGFP)* embryos at 60 hpf. The white arrowhead indicates the ventricular cells derived from the SHF. (**P**) Schematic of *Tg(atf3:RFP2Acre)* driver and *Tg(ubiquitin:CSY)* reporter transgenes. Lineage tracing analysis of *atf3*$^+$ cells by *Tg(atf3:RFP2Acre);Tg(ubiquitin:CSY)* at 60 hpf. A, atrium. $n \geq 30$ embryos per group for WISH and fluorescence observation. Scale bars, 50 μm.

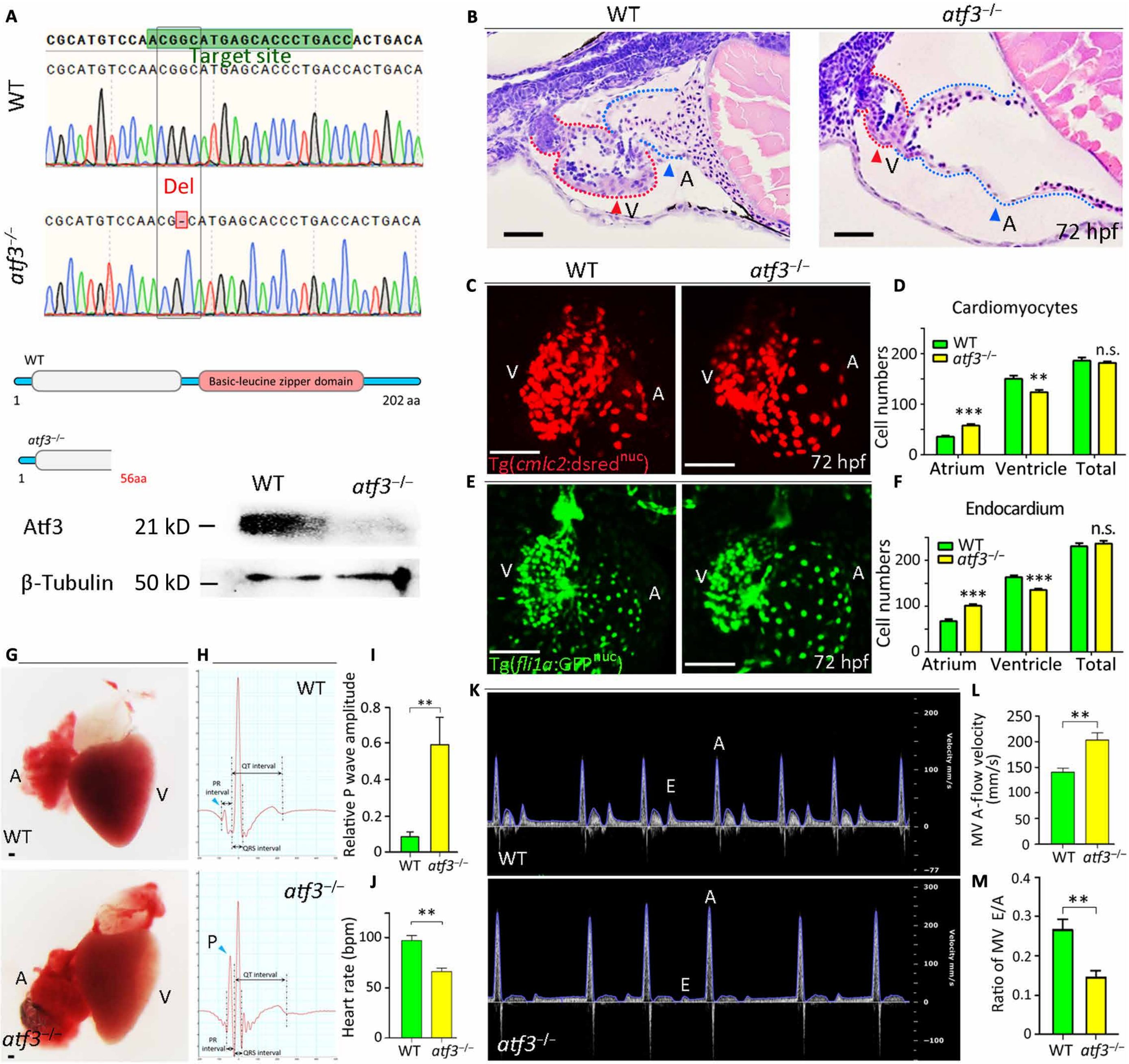

Fig. 2. Loss of *atf3* caused dilated atrial cardiomyopathy. (**A**) Genomic sequences of *atf3* in the wild-type (WT) and homozygous mutant zebrafish and the schematic diagram of truncated Atf3 protein of the homozygous mutants. Loss of one base pair in exon 2 led to the formation of an early stop codon. Atf3 protein was detected in the WT and mutant embryos by Western blot at 24 hpf. (**B**) Hematoxylin and eosin staining of transverse sections of hearts (6 μm thick per section, $n \geq 6$ embryos per group) at 72 hpf. (**C**) Confocal images of embryonic hearts in the *Tg(cmlc2:dsRed^{nuc})* control line and the *atf3$^{-/-}$;Tg(cmlc2:dsRed^{nuc})* line at 72 hpf. (**D**) Statistical analysis of the cell number of cardiomyocytes in the control and *atf3$^{-/-}$* embryos in (C) ($n \geq 6$). (**E**) Confocal images of embryonic hearts in the *Tg(fli1a:eGFP^{nuc})* control line and the *atf3$^{-/-}$;Tg(fli1a:eGFP^{nuc})* line at 72 hpf. (**F**) The endocardial cell counts in the control and *atf3$^{-/-}$* embryos in (E) ($n \geq 6$). (**G**) Morphology of WT and *atf3$^{-/-}$* adult (1-year-old) zebrafish heart ($n \geq 6$). (**H**) The electrocardiography waveform average of 5-min recorded data. Blue arrowhead indicates the P wave. (**I**) P wave amplitude relative to the QRS amplitude ($n \geq 6$ adults per group). (**J**) Heart rates of the adult WT and *atf3$^{-/-}$* adult zebrafish ($n \geq 6$). (**K**) Pulse-wave Doppler image of ventricular inflow of adult (5-month-old) WT and *atf3$^{-/-}$* zebrafish. The *y* axis indicates velocity (mm/s), and the *x* axis indicates time (ms). (**L**) The velocity of A-flow ($n \geq 6$ fish per group). (**M**) Assessment of diastolic dysfunction by mitral valve (MV) E/A ratio ($n \geq 6$ per group). Statistical analysis was carried out using the unpaired two-tailed Student's *t* test. Error bars indicate SD. n.s., $P > 0.05$, $^{**}P < 0.01$, $^{***}P < 0.001$. Scale bars, 50 μm.

fivefold increase in *atf3*$^{-/-}$ adults compared with the controls (Fig. 2, H and I), comparable to the peaked P wave observed in human CHD with right atrial enlargement. The heart rate of *atf3*$^{-/-}$ adults was 31.4% slower than that of the controls, indicating bradycardia (Fig. 2J). Echocardiography assessment showed that the velocity of A-flow (atrial component of ventricular filling) was significantly augmented by 44.0%, while the velocity of E-flow (early ventricular filling) was slightly decreased in *atf3*$^{-/-}$ adults compared with the WT controls (Fig. 2, K and L). The increased velocity of A-flow and the decreased E/A ratio (Fig. 2M) in *atf3*$^{-/-}$ mutants suggested that *atf3* deficiency caused atrial overload, which is a risk factor of early heart failure. These data demonstrated that *atf3* is a critical regulator of embryonic cardiac development and/or adult cardiac function.

Loss of *atf3* impairs differentiation of both CPs and HPs

While exploring the cellular mechanisms underlying the defect in the establishment of the chamber proportion in the *atf3*$^{-/-}$ mutant heart, we found enhanced expression of the atrial marker *amhc* and decreased expression of the ventricular marker *vmhc* in *atf3*$^{-/-}$ embryos at 22 ss (Fig. 3, A to D), suggesting an alteration in ventricular-atrial fate of CPs in the FHF. Meanwhile, the *ltbp3*-marked SHF remained unchanged at 26 hpf (fig. S3A). We first localized the ALPM by detecting mRNA expression of the ALPM marker *gata4* (*16*) at 9 ss. Although the entire ALPM remained intact in the *atf3*$^{-/-}$ embryos, its caudal portion expanded evidently compared with the control (Fig. 3, E and F). We further localized the cardiac fields by detecting *nkx2.5* and *hand2* mRNA expression in the ALPM. In comparison with the long narrow expression pattern in the WT controls, the expression of both *nkx2.5* and *hand2* in the mutants was restricted to a shorter but wider region in the caudal portion of the ALPM (Fig. 3, E and F). Compared with the medial region within the ALPM, the bilateral region has a stronger tendency toward atrial specification (*1*), which may explain the expansion of *atf3*$^{-/-}$ atrial cardiomyocytes. In addition, loss of *atf3* led to increased expression levels of *gata4* but did not affect the total expression levels of *hand2* and *nkx2.5* at this stage (Fig. 3G). Hence, the deformed heart field may indicate the excessive expansion of atrial cells at the expense of ventricular potential of CPs. This might underlie the dilated atrial cardiomyopathy phenotype.

Notably, the area of adjacent *tal1*$^{+}$ HPs in the ALPM was expanded in the *atf3*$^{-/-}$ embryos at 9 ss (Fig. 3, H and J), compared with the WT controls. Consequently, *pu.1*$^{+}$ primitive myeloid progenitors (Fig. 3, I and K) and *mpx*$^{+}$ neutrophils/monocytes (Fig. 3, L and M) were increased in the *atf3*$^{-/-}$ embryos. In addition, *tal1*$^{+}$ HPs in the intermediate cell mass (ICM) and *gata1*$^{+}$ primitive erythroid progenitors (fig. S3, B and D) were increased in the *atf3*$^{-/-}$ embryos at 22 hpf compared with the WT controls. A similar phenotype was observed in the definitive hematopoiesis as *runx1*$^{+}$ and *c-myb*$^{+}$ HSCs, α*e1*$^{+}$ erythrocytes, and *rag1*$^{+}$ lymphoid progenitors were increased in *atf3*$^{-/-}$ embryos (fig. S3, C and D) compared with the WT controls.

Furthermore, morphological analysis of blood cells in the *atf3*$^{-/-}$ kidney marrow (KM) showed a higher proportion of precursors and immature myeloid cells with large cytoplasm and incompact nuclei compared with the control (Fig. 3, N and O). Flow cytometry analysis of the KM showed that the percentage of precursors in the KM of *atf3*$^{-/-}$ fish was significantly increased, while the number of mature lymphoid and myeloid compartments was decreased compared with the controls (Fig. 3P and fig. S3E). The number of myelomonocytes was decreased in the *atf3*$^{-/-}$ mutants, as assessed by granularity analysis (fig. S3F), implying a blockade of myeloid maturation. The presence of excessive immature myeloid cells in *atf3*$^{-/-}$ mutants resembles a myeloid leukemia–like symptom. The coexistence of congenital cardiac defects and hematopoietic disorders in *atf3*$^{-/-}$ fish may have important clinical relevance, as a similar phenotype has been observed in human patients (*2*–*4*). In addition, the expression levels of the endothelial markers *tie1* and *flk1* and the endocardium marker *nfatc1* exhibited no significant change in *atf3*$^{-/-}$ embryos (fig. S4, G to I).

atf3 autonomously regulates differentiation of CPs and HPs

We further sought to understand the cell type–specific roles of Atf3 in HPs and CPs. A truncated form of *atf3*, lacking the C-terminal activation domain, termed *atf3*$^{\Delta \text{zip}}$, is expressed in the *tal1*$^{+}$ HPs and *nkx2.5*$^{+}$ CPs under control of the *tal1* promoter (*17*) and the *nkx2.5* promoter, respectively (*18*) (Fig. 4A). The truncated Atf3 protein acts as a dominant negative (DN) inhibitor, based on previous reports (*19*). We confirmed that *atf3*$^{\Delta \text{zip}}$ induced a similar heart defect phenotype as observed in *atf3*$^{-/-}$ mutants (Fig. 4B). The stable transgenic lines showed that the *tal1* promoter–driven *atf3*$^{\Delta \text{zip}}$ was specifically expressed in HPs, as shown by eGFP fluorescence in the ICM at 22 hpf (Fig. 4C), and the *nkx2.5* promoter–driven *atf3*$^{\Delta \text{zip}}$ was expressed with high fidelity in the heart and PAAs at 48 hpf (Fig. 4D).

The specific inhibition of Atf3 either in *tal1*$^{+}$ HPs or in *nkx2.5*$^{+}$ CPs activated the expression of *tal1* (Fig. 4, E and G) and restricted the expression region of *nkx2.5* to a shorter but wider region in the caudal portion of the ALPM (Fig. 4, F and H). Hence, *atf3* autonomously regulated differentiation of CPs and HPs. Because of the known antagonism between CPs and HPs in the ALPM, the change of one progenitor population could consequently affect the other. The data further showed that the hematopoietic- and cardiac-specific *atf3* changes resulted in atrial dilation both at 72 hpf (fig. S4, A and B) and in adults (fig. S4, C and D), and in increased *pu.1*$^{+}$ myeloid progenitors at 22 hpf (fig. S4, E and F) and hematopoietic precursors in adults (fig. S4G). The phenotypes seen in *atf3*-deficient animals were rather marked during early development and seemed to be partially compensated for in adults.

Notably, the cell type–specific manipulation also led to tissue-specific phenotypes. The cardiac defect in animals with cardiac *nkx2.5*-Δ*atf3* was stronger than in those with *tal1*-Δ*atf3*, while the hematopoietic-specific *tal1*-Δ*atf3* resulted in a stronger phenotype in the hematopoietic lineage (Fig. 4, E to H, and fig. S4). After the period during which CPs and HPs are closely related in the ALPM, *nkx2.5*-Δ*atf3* did no longer block HP differentiation. Hence, a higher ratio of myeloid cells was detected in *nkx2.5*-Δ*atf3* adults compared with controls (fig. S4H). In addition, no significant quantitative change of proliferating CPs was found between *atf3*$^{-/-}$ mutants and the control group, based on bromodeoxyuridine (BrdU) incorporation assays (fig. S5, A and B). These results demonstrated that *atf3* plays a regulatory role in the differentiation of both CPs and HPs.

atf3 mediates the *nkx2.5*-*tal1* interplay

To gain insight into the underlying molecular mechanisms, we performed morpholino (MO) knockdown of *tal1* in WT and *atf3*$^{-/-}$ embryos and found that loss of *tal1* could partially restore the expression pattern of *nkx2.5* (Fig. 4, I and J) and rescue the atrial

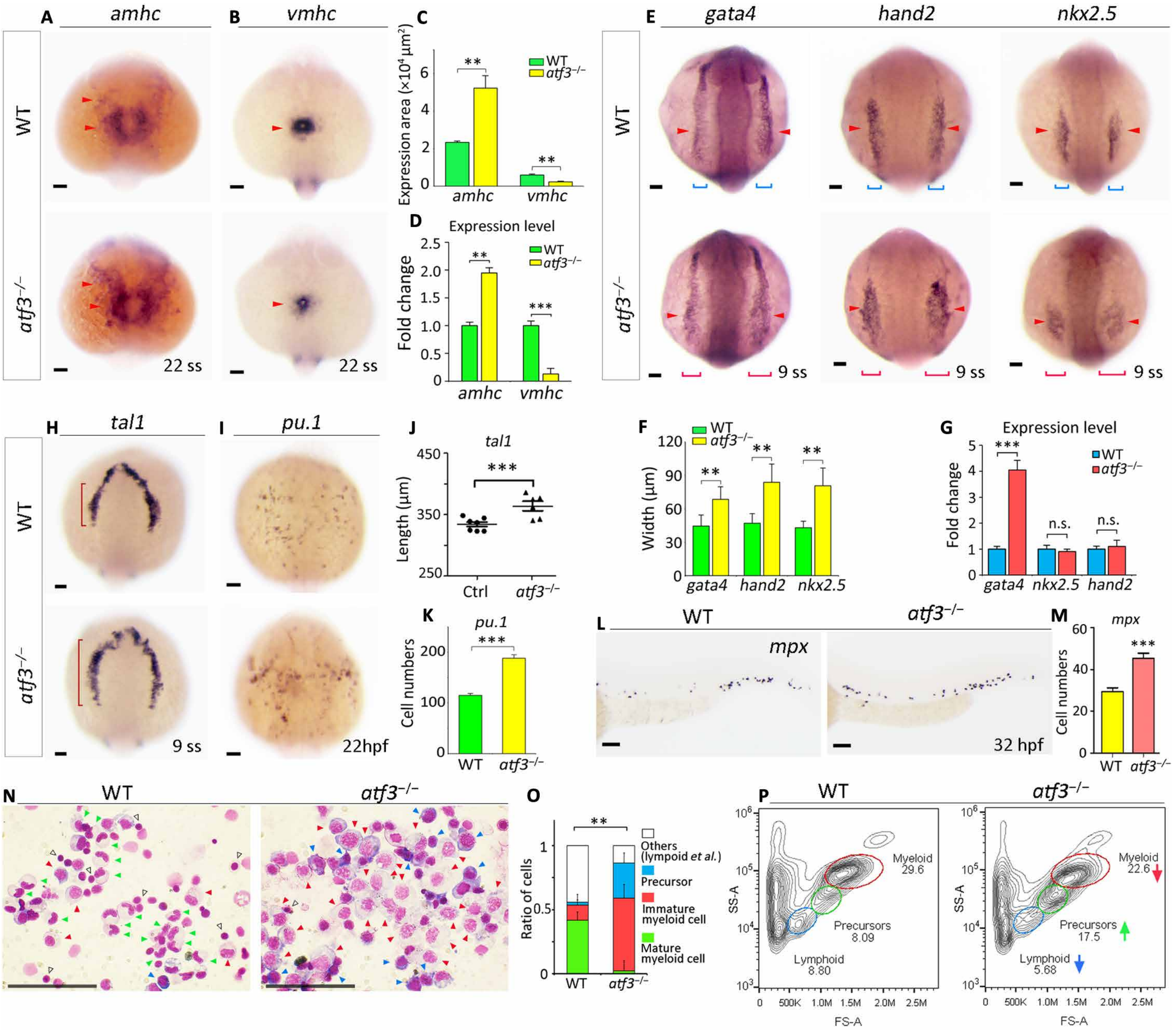

Fig. 3. Deficiency of *atf3* impaired differentiation of both CPs and HPs. (**A** and **B**) WISH of atrial (*amhc*) and ventricular (*vmhc*) lineage markers in the WT and *atf3*$^{-/-}$ embryos at 22 ss ($n = 21$ for WT and $n = 16$ for *atf3*$^{-/-}$ embryos in the WISH of *amhc*; $n = 23$ for WT and $n = 21$ for *atf3*$^{-/-}$ embryos in the WISH of *vmhc*). (**C**) Statistical analysis of the expression area of *amhc* and *vmhc* ($n = 16$ per group), using the unpaired two-tailed Student's *t* test. $^{**}P < 0.01$. (**D**) Relative mRNA expression levels of *amhc* and *vmhc* in WT and *atf3*$^{-/-}$ embryos at 22 ss ($n = 6$). Statistical analysis was carried out using the unpaired two-tailed Student's *t* test. $^{**}P < 0.01$, $^{***}P < 0.001$. (**E**) WISH of the ALPM marker *gata4* ($n = 29$ for WT, $n = 15$ for *atf3*$^{-/-}$ embryos), the heart-forming region marker *hand2* ($n = 29$ for WT, $n = 38$ for *atf3*$^{-/-}$ embryos), and the CP marker *nkx2.5* ($n = 20$ for WT, $n = 15$ for *atf3*$^{-/-}$ embryos) at 9 ss. Arrowheads indicate the specific expression patterns of the markers. The brackets indicate the width of the expression pattern in the ALPM. (**F**) The width of the expression region of *gata4*, *hand2*, and *nkx2.5* in the ALPM ($n = 15$ per group). Statistical analysis was carried out using the unpaired two-tailed Student's *t* test. Error bars indicate SD. $^{**}P < 0.01$. (**G**) The relative mRNA expression levels of *gata4*, *hand2*, and *nkx2.5* in WT and *atf3*$^{-/-}$ embryos at 9 ss ($n = 6$). Statistical analysis was carried out using the unpaired two-tailed Student's *t* test. n.s., $P > 0.05$, $^{***}P < 0.001$. (**H**) Expression of *tal1* at 9 ss ($n = 30$ per group). The red brackets indicate the length of the *tal1* expression region in the ALPM. (**I**) Expression of *pu.1* ($n = 30$ per group). (**J**) Statistical analysis of the length of the expression region of *tal1* in (H) ($n \geq 6$ per group) using the unpaired two-tailed Student's *t* test. $^{***}P < 0.001$. (**K**) Counts of *pu.1*$^{+}$ cells in (I) ($n \geq 6$ per group). (**L**) Expression pattern of *mpx* at 32 hpf ($n = 30$ per group). (**M**) Counts of *mpx*$^{+}$ cells in (L) ($n = 30$ per group). Statistical analysis was carried out using the unpaired two-tailed Student's *t* test. $^{***}P < 0.001$. (**N**) Wright-Giemsa staining of (1-year-old) KM cells after cytospin process ($n = 6$ per group). Green arrowheads indicate mature myeloid cells, red arrowheads indicate immature myeloid cells, blue arrowheads indicate precursors, and hollow arrowheads indicate other cells, such as lymphoid cells. (**O**) Ratios of different blood cell types in the KM of WT and *atf3*$^{-/-}$ zebrafish ($n = 6$ per group). Statistical analysis was carried out using the Kruskal-Wallis test with adjustments for multiple comparisons. $^{**}P < 0.01$. SS-A, side scatter-axis; FS-A, forward scatter-axis. (**P**) Flow cytometry analysis of the KM cells of adult (5-month-old) WT and *atf3*$^{-/-}$ zebrafish ($n = 6$ per group). Scale bars, 50 µm.

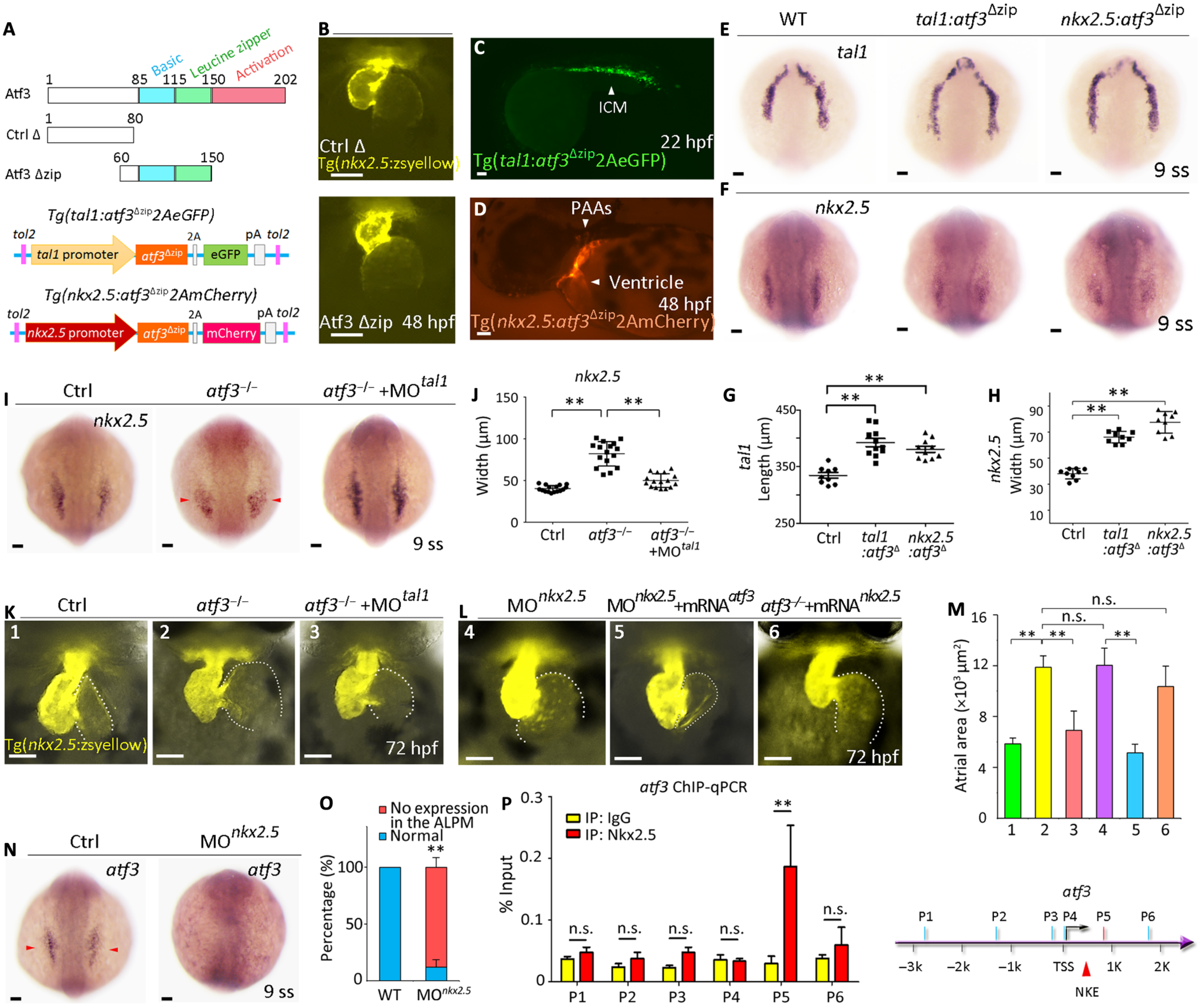

Fig. 4. *atf3* autonomously regulated differentiation and mediated the interaction between *nkx2.5* and *tal1*. (**A**) Top: Schematic diagram showing a control fraction of *atf3* (Ctrl Δ) and a truncated form of *atf3* bereft of the C-terminal activation domain (Atf3 Δzip) acting as a DN inhibitor, based on previous reports. Bottom: *tol2*-mediated transgenesis of *tal1* and *nkx2.5* promoting *atf3*$^{\Delta zip}$-eGFP and mCherry expression, respectively. (**B**) Morphological analysis of the embryonic heart in *Tg(nkx2.5:ZsYellow)* embryos with control *atf3*Δ mRNA injection and *Tg(nkx2.5:ZsYellow)* embryos with *atf3*Δzip mRNA injection at 48 hpf ($n = 30$ per group). (**C**) Expression pattern of fluorescence in ICM of the *Tg(scl:atf3*$^{\Delta zip}$*-eGFP)* stable line at 22 hpf ($n = 30$). (**D**) Expression pattern of fluorescence in the ventricle and PAAs of the *Tg(nkx2.5:atf3*$^{\Delta zip}$*-mCherry)* stable line at 48 hpf ($n = 30$). (**E**) Expression patterns of *tal1* in WT, *Tg(tal1: atf3*$^{\Delta zip}$*2AeGFP)*, and *Tg(nkx2.5: atf3*$^{\Delta zip}$*2AmCherry)* embryos at 9 ss ($n \geq 30$ per group). (**F**) Expression patterns of *nkx2.5* in WT, *Tg(tal1: atf3*$^{\Delta zip}$*2AeGFP)*, and *Tg(nkx2.5: atf3*$^{\Delta zip}$*2AmCherry)* embryos at 9 ss ($n \geq 30$ per group). (**G**) Statistical analysis of the length of the expression pattern of *tal1* in (E) ($n \geq 9$ for each group), using the Kruskal-Wallis test. Error bars indicated SD. $^{**}P < 0.01$. (**H**) Statistical analysis of the width of the expression region of *nkx2.5* in (F) ($n \geq 9$ per group), using the unpaired two-tailed Student's *t* test. $^{**}P < 0.01$. (**I**) Expression region of *nkx2.5* in the control embryos, *atf3*$^{-/-}$ embryos, and *atf3*$^{-/-}$ embryos with MO^{tal1} injection at 9 ss ($n \geq 35$ per group). (**J**) Statistical analysis of the width of the expression region of *nkx2.5* ($n = 16$ per group), using the unpaired two-tailed Student's *t* test. $^{**}P < 0.01$. (**K** and **L**) Morphological analysis of the embryonic heart in the control embryos (1), *atf3*$^{-/-}$;*Tg(nkx2.5:ZsYellow)* embryos (2), *Tg(nkx2.5:ZsYellow)* embryos with MO^{tal1} injection (3), *Tg(nkx2.5:ZsYellow)* embryos with MO$^{nkx2.5}$ (4), *Tg(nkx2.5:ZsYellow)* embryos with MO$^{nkx2.5}$ and mRNA^{atf3} coinjection (5), and *atf3*$^{-/-}$;*Tg(nkx2.5:ZsYellow)* embryos with mRNA$^{nkx2.5}$ injection (6) at 72 hpf ($n \geq 30$ per group). The dashed line outlines the atrium. (**M**) Statistical analysis of the atrial area in (K, 1 to 3) and (L, 4 to 6) ($n = 20$ per group), using the unpaired Student's two-tailed *t* test. Error bars indicate SD. n.s., $P > 0.05$, $^{**}P < 0.01$. (**N**) WISH of *atf3* in the control and embryos with MO$^{nkx2.5}$ injection at 9 ss ($n = 40$ per group). (**O**) Percentage of the differential expression of *atf3* ($n = 6$, 30 embryos per test). Statistical analysis was carried out using the Kruskal-Wallis test with adjustments for multiple comparisons. $^{**}P < 0.01$. (**P**) Binding enrichment region at the *atf3* locus as indicated by primers P1 to P6. The minimal DNA binding consensus for Nkx2.5 contained a 5′-TNNAGTG-3′ sequence motif, indicated by the red arrowhead. The ChIP analysis was performed with anti-Nkx2.5 antibody for the promoter region of *atf3* in WT embryos at 9 ss ($n = 6$, 100 embryos per group per experiment). Error bars indicate SD. Statistical analysis was carried out using the unpaired two-tailed Student's *t* test. n.s., $P > 0.05$, $^{**}P < 0.01$. Scale bars, 50 μm. IgG, immunoglobulin G.

dilation phenotype in *atf3*$^{-/-}$ mutants (Fig. 4, K and M). Therefore, *atf3* appears to function upstream of *tal1*. It has been reported that embryos lacking *nkx2.5* have a small ventricle and an enlarged atrium (*20*), quite similar to *atf3*$^{-/-}$ embryos (Fig. 4, K1, L, and M). Notably, we found that loss of *nkx2.5* led to the absence of *atf3* transcripts in the ALPM (Fig. 4, N and O), suggesting that *nkx2.5* may signal through *atf3*. These cardiac defects in the *nkx2.5* morphant could be rescued by restoring the expression of *atf3* (using a validated *atf3* mRNA, fig. S5, C and D), but the introduction of *nkx2.5* mRNA failed to rescue the cardiac defects in *atf3*$^{-/-}$ fish (Fig. 4, K1, L, and M). These studies indicated that, in the regulation of cardiac development, *atf3* is a downstream mediator of *nkx2.5*. Last, to analyze whether *atf3* is a direct transcriptional target of *nkx2.5*, we located the Nkx2.5-binding element (*21*) in the promoter region of *atf3* and performed chromatin immunoprecipitation (ChIP) with quantitative polymerase chain reaction (qPCR) to show the specific binding of Nkx2.5 at this locus (Fig. 4P). We confirmed that *atf3* is a gene downstream of *nkx2.5*. Collectively, our data showed that *atf3* regulates the functional antagonistic interplay between *nkx2.5* and *tal1* by positively responding to *nkx2.5* and transcriptionally suppressing *tal1*.

atf3 primarily targets *cebpγ*, negatively regulating its expression

To fully understand the role of *atf3* in CP/HP development, we performed an unbiased genome-wide ChIP sequencing assay of Atf3 to explore its potential targets. The distribution regions of Atf3 binding peaks in the genome are shown in Fig. 5A. Gene set enrichment analysis revealed that *atf3*-targeted genes were enriched in the biological processes of, among others, leukemia, cardiomyopathy, and diabetes (Fig. 5B). Notably, the gene encoding CCAAT/enhancer binding protein γ (*cebpγ*) was the top-ranked target, with high enrichment of Atf3 binding in the promoter region (Fig. 5C). As an autoregulatory transcription factor, Atf3 could bind its own promoter (Fig. 5C). Atf3 binding profiles in the promoter regions of *cebpγ* and *atf3* are visualized in Fig. 5D. As the chronic myeloid leukemia signaling pathway has the highest enrichment score, major genes in this pathway were analyzed by unsupervised hierarchy clustering. The heat map showed that the binding of Atf3 was highly enriched within their regulatory regions, especially that of *cebpγ* (Fig. 5E). Notably, loss of *atf3* in the mutants caused higher expression of *cebpγ* in the HP and CP regions at 9 ss (Fig. 5F) and in the heart tube at 24 hpf (Fig. 5G) compared with the WT controls, indicating a negative regulatory role of *atf3* in the expression of *cebpγ*. The differential expression of *cebpγ* between *atf3*$^{-/-}$ mutants and WT controls was most significant at the early embryonic stages (9 ss and 24 hpf) (Fig. 5H).

Regarding cardiogenesis, we found that overexpression of *cebpγ* resulted in a compressed expression region of *nkx2.5* (Fig. 5, I and L) and a dilated atrium (Fig. 5, J and M), phenotypes similar to those of *atf3*$^{-/-}$ mutants. Conversely, knockdown of *cebpγ* elongated the expression region of *nkx2.5* and *hand2* (fig. S6, A to D) and rescued the cardiac defects in *atf3*$^{-/-}$ mutants (Fig. 5, I, J, L, and M). Regarding hematopoiesis, overexpression of *cebpγ* led to the elongated expression pattern of *tal1* (Fig. 5, K and N), and knockdown of *cebpγ* inhibited the expression of *tal1* (fig. S6, E and F) and restored the defect in *atf3*$^{-/-}$ mutants (Fig. 5, K and N). In addition, knockdown or overexpression of *cebpγ* transcripts did not affect the expression levels of *nkx2.5* and *hand2* (fig. S6G). Hence, *cebpγ* could directly mediate the role of *atf3* in regulating differentiation of CPs and HPs.

Atf3 attenuates glucose metabolism by repressing *Cebpγ-Glut1a*

C/EBP is known to be a key regulator of glucose metabolism and can directly bind to the promoters of glucose transporter genes (*22*). Since the glucose transporter *Slc2a1/Glut1* is the predominant isoform in the fetus, we confirmed that *Slc2a1* transcripts were highly enriched in the mesoderm, embryonic heart, and HSCs in mouse, compared with ectodermal cells (Fig. 6A), and *slc2a1a* was also enriched in the *nkx2.5*$^{+}$ CPs in zebrafish (Fig. 6B). The overexpression of *cebpγ* or loss of *atf3* resulted in the elevated expression of *slc2a1a* and phosphoenolpyruvate carboxykinase 1 (*pck1*) at 9 ss, but not *slc2a1b*, compared with the controls (Fig. 6C), suggesting that *atf3* could limit glucose metabolism by inhibiting *cebpγ*-dependent glucose uptake. We located four putative CCAAT/enhancer binding protein (CEBP) binding sites (CCAAT) in the promoter region of *slc2a1a* (fig. S7, A and B), and by ChIP-qPCR assay, we found that Cebpγ binding peaks were highly enriched in the two loci of CEBP binding sites in the WT controls, and the binding of Cebpγ in the *slc2a1a* promoter was further increased in the *atf3*$^{-/-}$ mutants (Fig. 6D).

To extend our fish-based study to a mammalian system, we performed transcriptomic analysis using H9c2 mouse cardiac myoblast cells with or without *Atf3* deficiency and found 5793 annotated genes with differential expression. Consistent with the glucose metabolism data in fish, the *Atf3*-deficient group exhibited a significant increase in the positive regulation of glucose transport signaling (Fig. 6, E and F). Notably, among the genes that participate in this signaling, the expression of Ptpn11, whose gain-of-function mutation is known to cause the Noonan syndrome, was highly up-regulated upon *Atf3* deficiency (Fig. 6F). Consistent with the CP differentiation data in fish, the ventricular cardiac muscle development pathway was suppressed in the *Atf3*-deficient group (Fig. 6F).

As glucose metabolism is tightly coupled to progenitor differentiation, we wondered if *atf3* expression in CPs and HPs can respond to glucose levels. We found that the total expression of *atf3* was accordingly elevated in embryos upon the treatment with increasing doses of glucose (Fig. 6, G and H). Glucose treatment (2%) further enhanced the elongation of the *tal1* expression region (Fig. 6, I and J) and the compression of the *hand2* expression region (Fig. 6, K and L) in *atf3*-deficient embryos. Consequently, the heart abnormality was more severe in glucose-treated mutants (Fig. 6, M and N). Conversely, MO knockdown of *slc2a1a* (fig. S8A) could rescue the phenotypes of *atf3*$^{-/-}$ mutants (Fig. 6, I to N). Last, we found that oxygen consumption rates (oxidative phosphorylation) and extracellular acidification rates (glycolysis) were both significantly increased in the *atf3*$^{-/-}$ mutants compared with the WT control at 9 ss in the seahorse assay (Fig. 6O). We used the Slc2a1 inhibitor STF-31 ($C_{23}H_{25}N_3O_3S$) to reduce glucose metabolism. The data showed that a low dose of STF-31 could reverse the high mitochondrial and glycolytic activity in *atf3*$^{-/-}$ mutants (Fig. 6O). These results suggested that *atf3* could regulate glucose metabolism to provide adaptive capacity to high glucose levels.

Redox change causes the blockade of progenitor differentiation in *atf3*$^{-/-}$ mutants

The high levels of glucose metabolism due to the loss of *atf3* may alter the redox state and increase the levels of endoplasmic reticulum

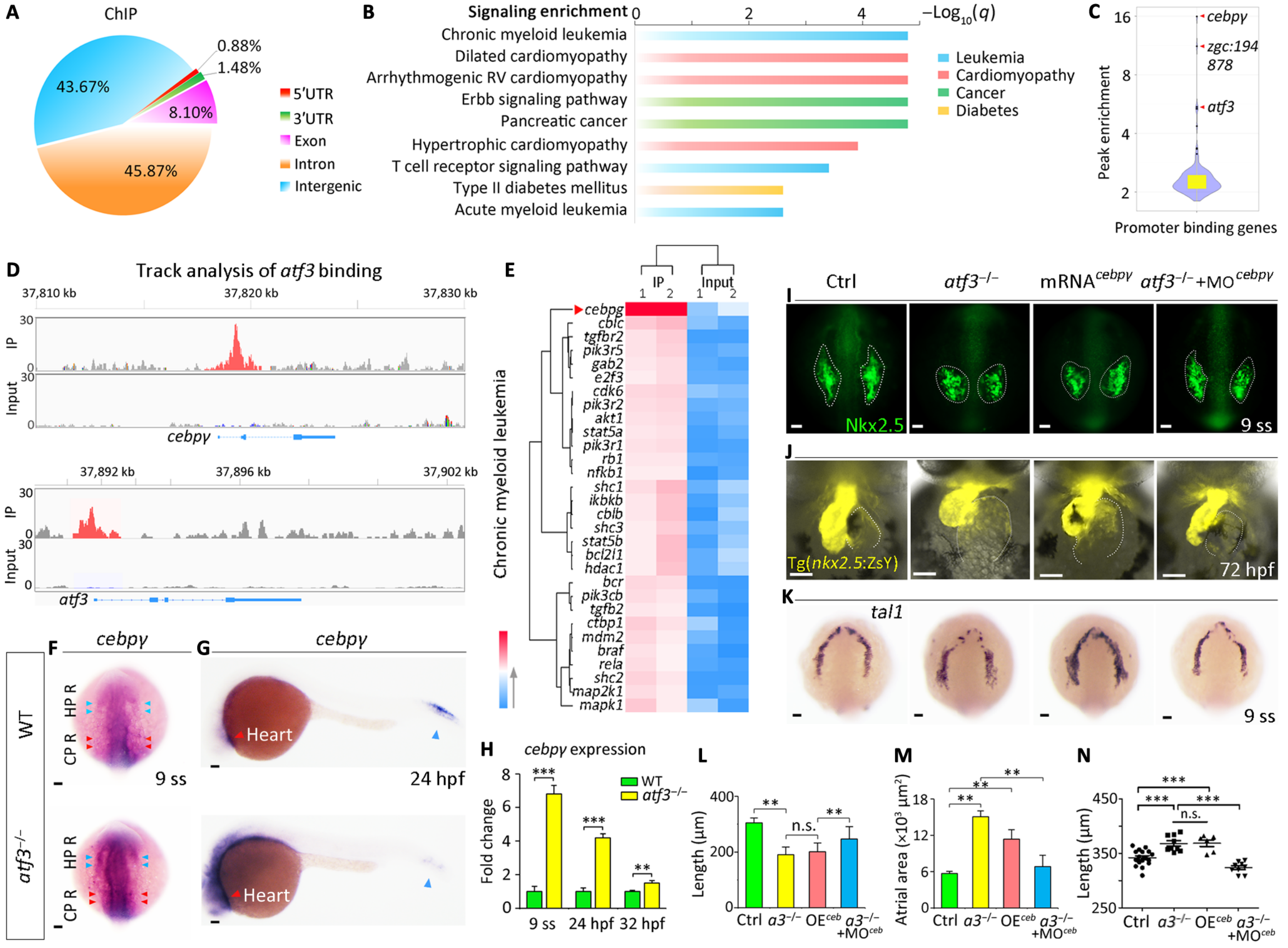

Fig. 5. *atf3* targeted *cebpγ*, negatively regulating its expression. (**A**) Genomic distribution regions of Atf3 binding peaks in the immunoprecipitated (IP) sample at 32 hpf. (**B**) Signaling pathway enrichment analysis of *atf3* binding by gene set enrichment analysis. RV, right ventricular. (**C**) Peak enrichment of *atf3* binding genes in IP samples in a violin-box plot. The red arrowheads indicate the top-ranked genes (duplicates per group). (**D**) Track analysis of Atf3 binding profiles in the promoter regions of *cebpγ* and *atf3*. (**E**) Major genes of the chronic myeloid leukemia signaling pathway were analyzed by the unsupervised hierarchy clustering, shown in the heat map. (**F** and **G**) Expression of *cebpγ* in the WT and *atf3*$^{-/-}$ embryos at 9 ss and 24 hpf ($n = 35$ per group). Blue arrowheads indicate HP region, and red arrowheads indicate CP region. (**H**) Relative mRNA expression level of *cebpγ* in the WT and *atf3*$^{-/-}$ embryos ($n = 30$ per group). Statistical analysis was carried out using the unpaired two-tailed Student's *t* test. Error bars indicate SD. $^{**}P < 0.01$, $^{***}P < 0.001$. (**I**) Immunofluorescent staining of Nkx2.5 in the control embryos, *atf3*$^{-/-}$ embryos, WT embryos with mRNA$^{cebp\gamma}$ injection, and *atf3*$^{-/-}$ embryos with MO$^{cebp\gamma}$ injection at 9 ss ($n = 30$ per group). (**J**) Morphological analysis of the embryonic heart in the control embryos, *atf3*$^{-/-}$;*Tg(nkx2.5:ZsYellow)* embryos, *Tg(nkx2.5:ZsYellow)* embryos with mRNA$^{cebp\gamma}$ injection, and *atf3*$^{-/-}$; *Tg(nkx2.5:ZsYellow)* embryos with MO$^{cebp\gamma}$ injection at 72 hpf ($n = 30$ per group). (**K**) Expression of *tal1* in the control embryos, *atf3*$^{-/-}$ embryos, WT embryos with mRNA$^{cebp\gamma}$ injection, and *atf3*$^{-/-}$ embryos with MO$^{cebp\gamma}$ injection at 9 ss ($n = 56$ per group). (**L**) Statistical analysis of the length of the Nkx2.5 staining region in (I) ($n = 20$), using the unpaired two-tailed Student's *t* test. Error bars indicate SD. n.s., $P > 0.05$, $^{**}P < 0.01$. (**M**) Statistical analysis of the expression area of Nkx2.5 in the atrium in (J) ($n \geq 25$ per group), using the unpaired two-tailed Student's *t* test. Error bars indicate SD. $^{**}P < 0.01$. (**N**) Statistical analysis of the length of the expression region of *tal1* in (K) ($n \geq 6$ for each group), using the Kruskal-Wallis test. Error bars indicate SD, n.s., $P > 0.05$, $^{***}P < 0.001$. *a3*$^{-/-}$, *atf3*$^{-/-}$; OE^{ceb}, mRNA$^{cebp\gamma}$; MO^{ceb}, MO$^{cebp\gamma}$. Scale bars, 50 μm.

(ER) stress. Levels of NADPH (reduced nicotinamide adenine dinucleotide phosphate) oxidase 5 (*nox5*), which is responsible for oxidative stress, were increased in *atf3*$^{-/-}$ mutants, and expression of the reactive oxygen species scavenger glutathione peroxidase 3 (*gpx3*) was induced as well (Fig. 6P). Since glucose is a major energy source for the generation of NADP and NADPH for cell metabolism, the ratio of NADP/NADPH was measured. Deficiency of *atf3* led to an increase of NADP/NADPH ratio, indicating a decrease in redox potential (Fig. 6Q). These data suggested that loss of *atf3* altered the redox state. In addition, the expression levels of the unfolded protein response–related genes ER to nucleus signaling 1 (*ern1*) and apoptosis-related DNA damage inducible transcript 3 (*chop*) and the ER stress marker eukaryotic translation initiation factor 2 alpha kinase 3 (*perk*) were significantly increased in the *atf3*$^{-/-}$ mutants compared with the WT controls (Fig. 6R). Our Western blot data confirmed that Perk protein levels were elevated in *atf3*$^{-/-}$ and WT embryos after treatment with 2 mM H_2O_2 compared with the controls (Fig. 6S), indicating ER stress.

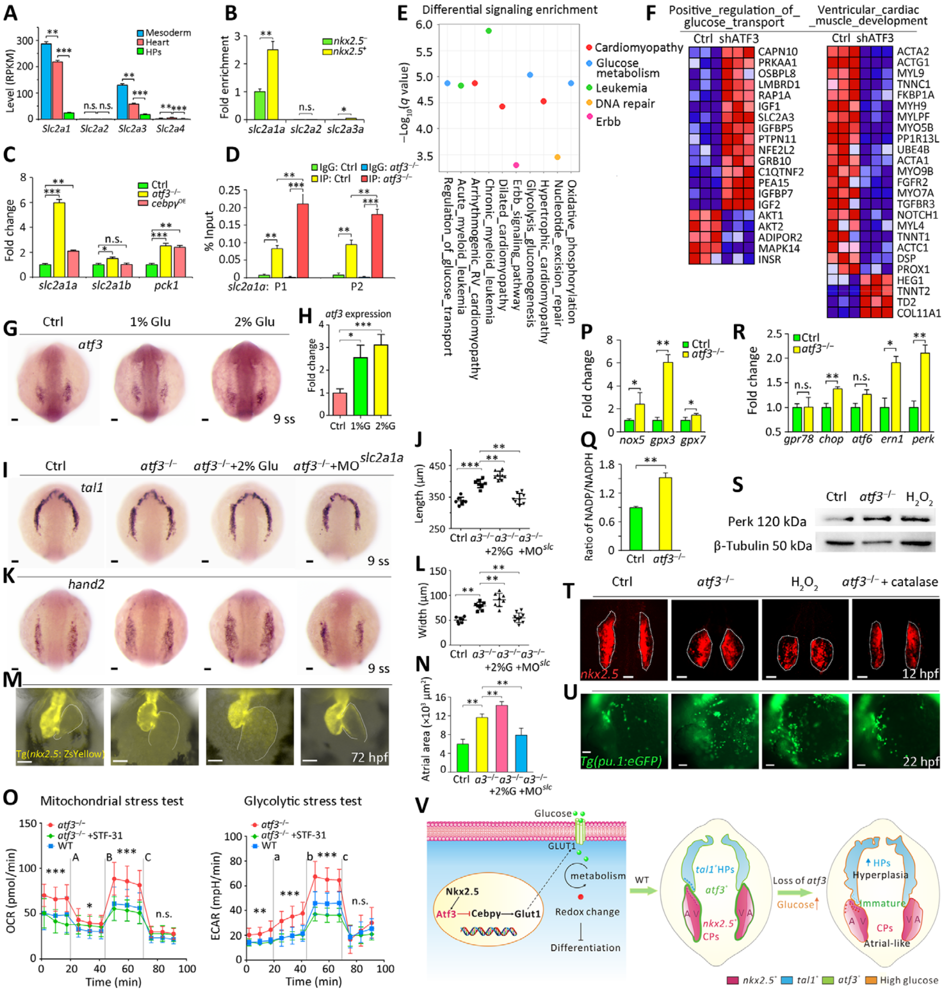

Fig. 6. *atf3-cebpγ* regulated glucose metabolism by targeting *glut1* and provided cells with adaptive capacity to high glucose levels. (**A**) The mRNA expression levels of *Slc2a1–4/Glut1–4* family members in the mouse mesoderm, the embryonic heart, and CD45$^+$CD144$^+$ HPs as analyzed by RNA sequencing (RNA-seq), relative to the expression in ectodermal cells ($n = 3$ per group). RPKM, reads per kilo base per million mapped reads. (**B**) Expression of *slc2a1–3/glut1–3* family members in *nkx2.5*$^+$ CPs and control cells in zebrafish at 9 ss ($n = 9$). (**C**) Relative mRNA expression levels of *glut1a*, *glut1b*, and *pck1* in the control, *atf3*$^{-/-}$ embryos, and WT embryos with *cebpγ* mRNA injection at 9 ss ($n = 6$). (A to C) Statistical analysis was carried out using the unpaired two-tailed Student's *t* test. Error bars indicate SD. n.s., $P > 0.05$, $^*P < 0.05$, $^{**}P < 0.01$, $^{***}P < 0.001$. (**D**) ChIP-qPCR analysis of Cebpγ binding in the promoter region of *glut1a* at 9 ss. The binding enrichment region at the *glut1a* locus was identified by primers P1 and P2 (fig. S7). The ChIP analysis with anti-Cebpγ for the promoter region of *glut1a* in the WT and *atf3*$^{-/-}$ embryos at 9 ss ($n = 6$, 100 embryos per group per experiment). Statistical analysis was carried out using analysis of variance (ANOVA) with multiple comparison post hoc test. $^{**}P < 0.01$, $^{***}P < 0.001$. (**E**) Difference in expression of genes encoding signaling proteins between the scramble and sh-*Atf3* H9c2 cell lines, as analyzed by RNA-seq ($n = 3$ per group). (**F**) Heat map of genes encoding proteins involved in the signaling pathways ($n = 3$ per group). (**G**) In situ hybridization analysis of the expression pattern of *atf3* in embryos treated with different doses of glucose at 9 ss ($n = 30$ per group). (**H**) The relative mRNA expression level of *atf3* in (G) ($n = 6$). Statistical analysis was carried out using the unpaired two-tailed Student's *t* test. Error bars indicate SD. $^*P < 0.05$, $^{***}P < 0.001$. (**I** and **K**) In situ hybridization analysis of the expression pattern of (I) *tal1* and (K) *hand2* in the control, *atf3*$^{-/-}$ embryos, *atf3*$^{-/-}$ embryos treated with glucose, and *atf3*$^{-/-}$ embryos treated with *slc2a1a* MO injection at 9 ss ($n = 20$ per group). (**J**) Statistical analysis of the length of the expression pattern of *tal1* in (I) ($n \geq 6$), using the Kruskal-Wallis test. $^{**}P < 0.01$, $^{***}P < 0.001$. *a3*$^{-/-}$, *atf3*$^{-/-}$; MO^{slc}, MO^{slc2a1a}. (**L**) Statistical analysis of the width of the expression region of *hand2* in (K) ($n \geq 6$), using the unpaired two-tailed Student's *t* test. Error bars indicate SD. $^{**}P < 0.01$. *a3*$^{-/-}$, *atf3*$^{-/-}$; MO^{slc}, MO^{slc2a1a}. (**M**) Morphological analysis of the embryonic heart in the control, *atf3*$^{-/-}$; *Tg(nkx2.5:ZsYellow)* embryos, *atf3*$^{-/-}$; *Tg(nkx2.5:ZsYellow)* embryos with 2% glucose treatment, and *atf3*$^{-/-}$; *Tg(nkx2.5:ZsYellow)* embryos with *slc2a1a* MO injection at 72 hpf ($n = 30$ per group). (**N**) Statistical analysis of the expression area of Nkx2.5 in the atrium in (M) ($n = 25$ per group), using the unpaired two-tailed Student's *t* test. Error bars indicate SD. $^{**}P < 0.01$. *a3*$^{-/-}$, *atf3*$^{-/-}$; MO^{slc}, MO^{slc2a1a}. (**O**) Oxygen consumption rates (OCR) (oxidative phosphorylation) and extracellular acidification rates (ECAR) (glycolysis) were examined in WT cells, *atf3*$^{-/-}$ cells, and *atf3*$^{-/-}$ cells treated with 10 μM of the *slc2a1* inhibitor STF-31 at 9 ss, as analyzed by seahorse assay ($n = 8$). Statistical analysis was carried out using the unpaired two-tailed Student's *t* test. Error bars indicate SD. n.s., $P > 0.05$, $^*P < 0.05$, $^{**}P < 0.01$, $^{***}P < 0.001$. A, oligomycin; B, FCCP; C, rotenone/antimycin A; a, glucose; b, oligomycin; c, 2-deoxyglucose. (**P** and **R**) Relative mRNA expression levels of oxidative and ER stress markers in the control and *atf3*$^{-/-}$ embryos at 9 ss ($n = 6$). (**Q**) NADP/NADPH ratios at 9 ss, measured by the Sigma NADP/NADPH Quantification Kit ($n = 6$). (P to R) Statistical analysis was carried out using the unpaired two-tailed Student's *t* test. Error bars indicate SD. n.s., $P > 0.05$, $^*P < 0.05$, $^{**}P < 0.01$. (**S**) Perk protein levels in the control embryos, *atf3*$^{-/-}$ embryos, and WT embryos treated with 2 mM H_2O_2 at 9 ss, as analyzed by Western blot. (**T**) Immunofluorescence staining of Nkx2.5 in the control, *atf3*$^{-/-}$ embryos, WT embryos treated with 2 mM H_2O_2, and *atf3*$^{-/-}$ embryos with catalase injection (350 ng per embryo) at 12 hpf ($n = 30$ per group). (**U**) *pu.1*$^+$ myeloid progenitors in the control embryos, *Tg(pu.1:eGFP);atf3*$^{-/-}$ embryos, *Tg(pu.1:eGFP)* embryos treated with H_2O_2, and *Tg(pu.1:eGFP);atf3*$^{-/-}$ embryos with catalase injection at 22 hpf ($n = 30$ per group). (**V**) Schematic representation of the role of *atf3* in the regulation of differentiation of CPs and HPs. Scale bars, 50 μm.

Treatment with 2 mM H_2O_2 can cause changes in the expression patterns of *nkx2.5* and *tal1* (Fig. 6T and fig. S8, B, D, and E) and lead to an increase of *pu.1*$^+$ myeloid cells (Fig. 6U and fig. S8C), as a similar phenotype has been observed in *atf3*$^{-/-}$ embryos. Catalase injection can rescue the phenotype of *atf3*$^{-/-}$ embryos, indicating a crucial role of redox modulation in progenitor differentiation (Fig. 6, T and U, and fig. S8, B to E). Hence, our data indicated that the increased oxidative levels and ER stress may lead to the blockade of progenitor differentiation. Collectively, these results demonstrated that, during the differentiation of progenitor cells (HPs/CPs), *atf3* may reprogram cellular glucose metabolism accordingly to properly provide energy and support a balanced redox state (Fig. 6V).

DISCUSSION

CPs and HPs with normal differentiation potential are essential to generate heart and blood cells and for the development of a well-formed circulation system. A previous study implied that CPs and HPs compete with each other to maintain their lineages (*6*). However, factors that reconcile their differentiation remain elusive. In this study, we identified *atf3* as a critical developmental regulator for both CPs and HPs. Deficiency of *atf3* led to elongation of the *tal1*$^+$ hemogenic region and the compression of the *nkx2.5*$^+$ FHF within the ALPM. Our findings indicated that the ectopic distribution of CPs and HPs in *atf3*$^{-/-}$ embryos was primarily caused by differentiation defects rather than the disequilibrium of lineage competition. The selective inhibition of Atf3 in either HPs or CPs could directly suppress their differentiation. The defect in ventricular potential and HP hyperplasia in the mesoderm may be manifestations of the differentiation blockade in CPs and HPs, respectively. Therefore, we identified a new *atf3*-mediated regulatory mechanism that coordinates the differentiation of CPs and HPs in the mesoderm.

In this study, we found that the fine-tuned regulation of glucose metabolism played a vital role in the development of the circulation system at early embryonic stages. Energy supply from glucose metabolism is indispensable for the development of progenitors. For example, glucose restriction has been shown to affect myoblast differentiation (*23*, *24*), and increased glucose levels induce adipogenic differentiation (*25*). However, excessive glycolysis may induce the mitochondrial electron transport chain to overproduce superoxide, which inhibits differentiation. Recent studies have revealed that, in pregnant women, elevated random plasma glucose levels during the first and second trimesters are directly correlated with an increased risk for CHD in offspring (*26*). High glucose levels induced by transforming growth factor–β1 could also increase the number of HPs (*27*). Meanwhile, enhanced glycolysis increases HSC numbers but inhibits hematopoietic differentiation (*28*). We found that *atf3* deficiency induced high rates of glucose utilization, which could contribute to the atrial dilated cardiomyopathy and myeloid leukemia–like symptoms in zebrafish. Our findings implied a protective role for *atf3* in glucose tolerance of progenitors at the early embryonic stage.

Studies on ATF3-deficient mice have shown several system defects, including increased airway hyperresponsiveness (*14*) and increased renal ischemia/reperfusion-induced mortality. Nevertheless, to date, heart defects in *Atf3* mutant mice have not been reported. Basal ATF3 expression remains low in most cell types in adult mice and is elevated in the case of stress stimuli and disease such as myocardial ischemia, cardiac hypertrophy, dilated cardiomyopathy, and inflammation. However, the function of ATF3 in the adult heart is still controversial. Herein, we report an essential role for *atf3* in regulating glucose metabolism. Previous studies have implied that *atf3* and glucose homeostasis are associated. For instance, ATF3 levels were increased under high-glucose conditions in primary pancreatic islets (*29*), and *Atf3* can mediate the hypoglycemic effects through the down-regulation of hepatic gluconeogenesis (*30*). In this study, we revealed that *atf3* represses the insulin-independent glucose utilization mediated by *cebpγ-glut1a* in the embryonic stage.

We identified *cebpγ* as the primary Atf3-binding target in this study. CEBPγ is known to play a suppressive role in regulating transcriptional activators in the CEBP family. CEBPγ-deficient mice show a high mortality rate within 48 hours after birth (*31*), limiting studies on the function of CEBPγ in the heart and blood development. It has been reported that erythroid-specific overexpression of *Cebpγ* represses fetal liver erythropoiesis in mice (*32*), while up-regulation of CEBPγ promotes myeloid differentiation arrest, leading to acute myeloid leukemia (*33*). We found hematopoietic hyperplasia and inhibited myeloid maturation in *atf3*$^{-/-}$ zebrafish with *cebpγ* up-regulation. Therefore, *cebpγ*, a direct target of *atf3*, is likely to mediate the counter-regulatory role of *atf3* in hematopoiesis.

Our data indicate that the *atf3-cebpγ* axis regulates glucose utilization in fish and mammalian cells. Consistent with our data, it has been reported that CEBPs are critical regulators of glucose transport, gluconeogenesis, triglyceride synthesis, and energy homeostasis (*22*). CEBPα-knockout mice do not store hepatic glycogen and lipid and die from hypoglycemia within 8 hours after birth (*34*). Similarly, 50% of all CEBPβ-knockout mice die early because of disturbances in glycogen mobilization and consequent hypoglycemia (*35*). It is known that CEBP plays a critical role in the regulation of the insulin-responsive GLUT4 (*36*). Mechanistically, we found that *cebpγ* directly targeted *glut1a*, the dominant GLUT isoform in the fetus, regulating glucose metabolism.

The ability to take up glucose in vertebrates is a fundamental property that has long been intriguing to both basic and clinical researchers. Abnormality of glucose uptake may induce various clinical manifestations. High glucose–mediated redox changes due to increased expression of *Glut1* may contribute to cardiac hypertrophy (*37*). GLUT1 inhibition reverses a hypermetabolic state in mouse models of myeloproliferative disorders (*38*). The proposed mechanisms for the high glucose–induced maladaptation might be associated with oxidative stress, enhanced mitochondrial electron transport chain flow, and changes in the redox potential. Similar redox effects have been found in other developmental systems (*39*). In the present study, we found that *atf3*$^{-/-}$ embryos exhibited increased oxidative levels, which might impair the differentiation potential of progenitor cells.

The main limitation of this study is that we cannot isolate and culture CPs in vitro, because CP markers remain controversial. Hence, we could not directly analyze the role of *atf3* in CPs in vitro. To overcome this difficulty, we had to use a validated DN form of *atf3* driven by the *nkx2.5* and *tal1* promoters to selectively knock down *atf3* signaling in CPs and HPs in vivo. By the analysis of stable fish lines, overexpression of DN *atf3* in either HPs or CPs could induce defects similar to those in *atf3*$^{-/-}$ mutants. Hence, *atf3* could directly regulate the differentiation of HPs and CPs. The H9c2 fetal mouse heart myoblast cell line is a cellular model for mammalian cardiac differentiation. We therefore used this cell line to validate the results from zebrafish studies. In conclusion, our study provides new insights into the role of *atf3* in the regulation of glucose metabolism in CPs and HPs, which may contribute to our understanding of the etiology of CHD.

MATERIALS AND METHODS

Mouse embryo microdissection and cell sorting

Mouse embryos free of the deciduum were rinsed in serum-free and Hepes-buffered Dulbecco's modified Eagle's medium and then incubated in 2.5% pancreatic/0.25% trypsin enzyme solution at 4°C for 15 min. The embryos were microdissected to isolate the mesodermal and ectodermal layers at E7.5, as previously described (*40*). The fetal heart tube with outflow tract at E9.5 and the AGM at E11.5 were also isolated by microdissection. Digested cells from AGM tissues were purified by Dynabeads CD45 (Life Technologies) and then sorted twice into lysis buffer using CD144 antibody (BD Biosciences). Samples were snap-frozen in liquid nitrogen and pulverized before RNA extraction. The protocol was approved by the Review Board on the Ethics of Animal Experiments of Shanghai Institutes for Biological Sciences.

Zebrafish line maintenance

WT Tuebingen strain and transgenic zebrafish lines, including *Tg(nkx2.5:ZsYellow)*, *Tg(cmlc2:eGFP)*, *Tg(cmlc2:dsRed*^{nuc}*)*, *Tg(ubiquitin:CSY)*, *Tg(fli1a:GFP*^{nuc}*)*, and *Tg(pu.1:eGFP)*, were raised under standard conditions. *Tg(ltbp3*:eGFP) were constructed as previously described. The zebrafish experiments were approved by the Review Board of Shanghai Institutes for Biological Sciences, Chinese Academy of Sciences (Shanghai, China).

Generation of the *Tg(atf3:RFP2Acre)* line and *atf3* mutant line

Tg(atf3:RFP2Acre) were constructed as previously described (*27*) using MultiSite Gateway Three-Fragment Vector Construction Kit (Invitrogen). The 6.3-kb promoter upstream of *atf3* translation start site (TSS) was cloned into pDestTol2pA2 followed by TagRFP2Acre cassette and polyA. The plasmid was injected into one–cell stage WT embryos at a dose of 15 ng/μl with capped transposase RNA at a dose of 7.5 ng/μl. The primer information is listed in table S2.

CRISPR-Cas9 target sites were designed using ZiFiT Targeter version 4.2. The selected Cas9 target site in *atf3* is illustrated in Fig. 2A. The templates of Cas9 guide RNAs (gRNAs) were cloned into pT7-gRNA plasmid offered by B. Zhang's Lab (Peking University). Oligonucleotide sequences for cloning of gRNAs were as follows: Sense, 5′-ataGGTCAGGGTGCTCATGCCGTgt-3′; Anti-sense, 5′-taaaacACGGCATGAGCACCCTGAC-3′. The gRNA was synthesized using an in vitro RNA synthesis kit (MAXIscript T7 Kit, Ambion, Thermo Fisher Scientific Inc., USA). One hundred picograms of gRNA and 300 pg of Cas9 mRNA were injected into WT embryos at the one-cell stage.

Generation of the *Tg(nkx2.5: atf3*$^{\triangle zip}$*-2AmCherry)* and *Tg(tal1: atf3*$^{\triangle zip}$*-2AeGFP)* stable lines

The 6.5-kb promoter upstream of *nkx2.5* TSS (*18*) and a 5.7-kb promoter upstream of *tal1* TSS (*17*) were cloned into pCS2+ followed by *atf3*$^{\triangle zip}$-2AmCherry and *atf3*$^{\triangle zip}$-2AeGFP flanking with *tol2* transposons, respectively. The coded protein of *atf3*$^{\triangle zip}$ was the truncated form bereft of the C-terminal activation domain, based on previous reports (*19*). The plasmids were injected into one–cell stage WT embryos at a dose of 20 ng/μl with capped transposase RNA at a dose of 10 ng/μl. The F_0 fish were screened to obtain the stable lines. The primer information is listed in table S2.

MOs, mRNA synthesis, microinjection, and chemical treatment

All MOs were ordered from Gene Tools (USA). MOs were injected at one-stage embryos to generate morphants at a dose of 2.44 ng for *cebpγ*, 2 ng for *nkx2.5*, and 1.83 ng for *tal1*. For mRNA synthesis, full-length complementary DNA (CDS) was cloned into pCS2+ hemagglutinin (HA) vector. Capped mRNA was synthesized using the mMESSAGE mMACHINE SP6 Kit (Ambion). The mRNAs were injected into one–cell stage zebrafish embryos at 150 pg per embryo for mRNA$^{cebp\gamma}$, 400 pg per embryo for mRNA$^{HA\text{-}atf3}$, and 200 pg per embryo for mRNA^{tal1}. Catalase (C3556, Sigma, USA) was injected at 350 ng per embryo. MO sequences and the primers used for mRNA synthesis are listed in table S2. D-Glucose was applied to the zebrafish embryos from fertilization to 9 ss, 24 or 72 hpf at a dose of 1 or 2%. STF-31 (S7931, Selleckchem, USA) was applied to the zebrafish embryos from fertilization to 9 ss at a dose of 10 μM.

RNA probes and whole-mount and two-color in situ hybridization

Probe sequences of *atf3* and *cebpγ* were cloned in the pCS2+ plasmid. Antisense RNA probes were transcribed using T3 polymerase (Ambion) with digoxigenin (DIG labeling mixture, Roche Applied Science, Mannheim, Germany)–labeled uridine triphosphate (UTP) or fluorescein (fluorescein labeling mixture, Roche Applied Science, Mannheim, Germany)–labeled UTP. The probe primers are listed in table S2.

WISH for the detection of gene expression was performed using DIG-labeled antisense RNA probes. Zebrafish embryos were collected and fixed in 4% paraformaldehyde (PFA), dehydrated with methanol, and stored at −20°C. Rehydrated embryos were digested with proteinase K and hybridized overnight at 70°C. After anti–DIG–alkaline phosphatase incubation, embryos were stained with nitro blue tetrazolium chloride/5-bromo-4-chloro-3′-indolyphosphate *p*-toluidine (NBT/BCIP; Roche Applied Science, Mannheim, Germany). Two-color in situ hybridization was carried out using DIG- and fluorescein-labeled probes and then stained with NBT/BCIP and 2-[4-iodophenyl]-3-[4-nitrophenyl]-5-phenyltetrazolium chloride/BCIP (INT/BCIP; Roche Applied Science, Mannheim, Germany).

Fluorescence in situ hybridization and immunofluorescence staining

Embryo fixation, proteinase K treatment, prehybridization, and hybridization were performed as WISH process. Embryos were incubated with anti–DIG-horseradish peroxidase (POD) overnight at 4°C. TSA Plus Fluorescein tyramide working solution (PerkinElmer, Waltham, MA) was used to develop the probe signal of *atf3*, followed by the immunofluorescence staining with anti-RCFP (1:50, Clontech) primary antibody and Alexa Fluor 546 donkey anti-rabbit immunoglobulin G (IgG; 1:500, Invitrogen, Carlsbad, CA). Images were captured by an Olympus FluoView FV1000 confocal microscope (Olympus, Tokyo, Japan).

Confocal fluorescent imaging

The transgenic embryos were mounted in 3% low–melting point agarose and imaged on an Olympus FluoView FV1000 scanning confocal microscope (Olympus, Tokyo, Japan). GFP and eGFP were excited with a 488-nm argon laser and imaged through a 505- to 536-nm filter. ZsYellow was excited with a 515-nm argon laser and imaged through a 530-nm long-pass filter. TagRFP and dsRed were excited with a 543-nm HeNe laser and imaged through a 560-nm long-pass filter. mCherry was excited with a 564-nm HeNe laser and imaged through a 595-nm filter. AmCyan was excited with a 405-nm blue-diode laser and imaged through a 475-nm long-pass filter. BrdU-positive cells, cardiomyocytes, and endocardium cells of *Tg(cmlc2:dsRed^{nuc})* and *Tg(fli1a:GFP^{nuc})* were counted in projections of *Z*-stack images, respectively.

ChIP sequencing assay and ChIP-qPCR

The ChIP assay was carried out within the WT and embryos with HA-*atf3* mRNA injection at 32 hpf. The sonicated DNA was precipitated by HA-tag (C29F4) rabbit monoclonal antibody (Cell Signaling Technology, 3724) or normal rabbit IgG (negative control; Cell Signaling Technology, 2729). Afterward, the precipitated DNA was collected by a QIAquick PCR Purification Kit (28104). The gene expression profiles were detected by deep sequencing. The deep sequencing and primary data analysis were performed by Shanghai Novel Bioinformatics, Ltd. The enrichment analysis of genes with *atf3*-enriched regions was performed by gene set enrichment analysis (Broad Institute, Cambridge, MA, USA) and two-sided Fisher's exact test.

ChIP-qPCR was carried out using the WT and *atf3*$^{-/-}$ embryos at 9 ss. The Cebpγ protein was immunoprecipitated by anti-CEBPγ antibody (Sigma, HPA012024). Normal rabbit IgG was used as the negative control. The Nkx2.5 protein was immunoprecipitated by anti-Nkx2.5 antibody (PA5-49431, Thermo Fisher Scientific Inc., USA). The precipitated DNA were purified and analyzed by qPCR for Cebpγ binding. Primers are listed in table S2.

RNA extraction and RNA-sequencing analysis

RNAs were extracted from the scramble and *sh-Atf3* H9c2 cells and other samples using the TRIzol reagent (Life Technologies) according to the manufacturer's instructions. RNA quality was determined with an Agilent 2100 Bioanalyzer. Samples were processed using the Illumina mRNASeq Sample Preparation Kit according to the manufacturer's protocol. Each RNA-sequencing library was paired-end sequenced using the Illumina HiSeq. Raw reads in FASTQ format were aligned to the rat genome using Tophat software. Transcript isoform assembly and abundance estimation were performed using Cufflinks and combined with gene annotations from the National Center for Biotechnology Information.

BrdU and immunostaining

Dechorionated *Tg(nkx2.5:zsYellow)* WT and *atf3*$^{-/-}$ embryos at 16 hpf were treated with a prechilled 10 mM working concentration of BrdU (Roche) in embryo medium for 30 min on ice, followed by incubation at 28.5°C for 5 min before fixation in 4% PFA. After dehydration and rehydration, the embryos were treated with Proteinase K (10 mg/ml) for 8 min at room temperature, followed by acetone treatment at −20°C for 30 min. The embryos were then treated with 2 N HCl for 1 hour at room temperature and stained with mouse anti-BrdU (Life Technologies) and anti-RCFP (Clontech) antibodies. After incubation with the block solution (PBS with 0.3% Triton X-100, 1% bovine serum albumen and 1% dimethyl sulfoxide), the embryos were incubated with anti-mouse Alexa Fluor 546 and anti-rabbit Alexa Fluor 488 antibodies (Life Technologies) and imaged with an Olympus FluoView FV1000 confocal microscope.

Histological analysis of zebrafish embryos

Histological analysis was performed as previously described (*15*). WT and *atf3*$^{-/-}$ embryos were collected and fixed in 4% PFA and dehydrated with ethanol. The JB-4 Embedding Kit (Sigma, EM0100) was used for infiltration and embedding into the plastic resin. Six-micrometer sections were cut using a Leica microtome (Leica Microsystems GmbH Wetzlar, Germany) and stained with hematoxylin and eosin.

Western blot analysis

Western blot was performed with standard protocols. Protein was prepared from zebrafish embryos at 9 ss and dissolved in 4× protein SDS–polyacrylamide gel electrophoresis Loading buffer (Takara). Atf3, Perk, and Slc2a1 were detected with anti-ATF3 (HPA001562, Sigma, USA), anti-PERK (C33E10, CST, USA), and anti-Slc2a1 (D3J3A, CST, USA) at a dilution of 1:1000, followed by incubation with an anti-rabbit IgG–horseradish peroxidase antibody (ab97069, Abcam, USA) at a dilution of 1:5000. β-Tubulin was used as the internal control using an anti-β–tubulin antibody (T6199, Sigma, USA), followed by an anti-mouse IgG antibody (62-6520, Invitrogen, USA) diluted 1:1000 and 1:5000 in the block solution, respectively.

Cytological analysis of whole KM

The zebrafish KM was dissected from WT and *atf3*$^{-/-}$ adult zebrafish, and then single-cell suspension was generated by pipetting and filtering through 40-μm cell strainers (BD). Flow cytometry analysis of KM was based on the forward scatter and side scatter with the CytoFLEX Flow Cytometer. Cytospin of KM cells was made by centrifugation at 800 rpm for 3 min onto glass slides in a Cytospin 4 cytocentrifuge (Shandon, Thermo Fisher Scientific Inc., USA). Wright-Giemsa staining of the cytospins was performed as per the manufacturer's instruction (Wright-Giemsa stain, BASO Diagnostics Inc., Zhuhai, China).

ECG recording and echocardiogram

Adult WT and *atf3*$^{-/-}$ zebrafish were anesthetized in 0.02% tricaine solution. The fish was placed on a damp sponge with the ventral side up. For ECG recording, two stainless steel electrodes were inserted into the muscle layer of the chest. The reference electrode was positioned along the midline posterior to the pelvic fin. ECG signals were amplified by a Model 3000 AC/DC differential amplifier (A-M Systems, WA, USA) with 100 gain value and filtered at 0.1 to 300 Hz. The signals were digitized by PowerLab (ADInstruments) and viewed using LabChart 8 (ADInstruments). We defined the ratio of P wave amplitude/QRS complex amplitude as "relative P wave amplitude" to avoid the fluctuations of absolute P wave amplitude among individual samples.

For echocardiogram, the ultrasound transducer (MS-550D) of a Vevo 770 device was fixed with a mechanical holder and contacted the chest of zebrafish from above. All fish were evaluated through the Vevo 2100 Imaging System (VisualSonics Inc., USA). The frequency for B-mode imaging was 40 MHz, and the frame rate was approximately 450 Hz. The frequencies for color Doppler and pulsed-wave Doppler were 32 MHz, and the frame rates were approximately 50 Hz. The pulse repetition frequency was 20 kHz. The wall filter frequency was 500 Hz. All the studies were performed at 28°C for less than 8 min.

Seahorse analysis

The blastomeres of embryos at 9 ss were separated from the yolk using deyolk buffer. Cells were digested with 0.25% trypsin/EDTA

(1 ml per 100 embryos) for 12 min at 28.5°C and passed through a 40-μm nylon mesh filter. Cell density of zebrafish embryonic cells was 2×10^5 cells per well. Gibco Leibovitz's L-15/10% FBS medium was used for the XF assay; sodium pyruvate (1 mM final concentration) and glucose (2.5 g/liter) were added before use. The Seahorse XF96 extracellular flux analyzer (Agilent) was used for the analysis. Further procedures followed the standard XF assay protocol.

Statistical analysis

All biological experiments were performed at least three times. GraphPad Prism 6 software and R were used to analyze the data. Quantitative data were presented as the means ± SD. The normality of data was examined by Shapiro-Wilk test. The data of normal distributions were analyzed by unpaired two-tailed Student's *t* test between two groups. The data of non-normal distributions were analyzed by Kruskal-Wallis test with adjustments for multiple comparisons. n.s., $P > 0.05$, $^{*}P < 0.05$, $^{**}P < 0.01$, $^{***}P < 0.001$. Dysmorphic animals due to unknown developmental delays were excluded equally from the control and experimental groups.

SUPPLEMENTARY MATERIALS

Supplementary material for this article is available at http://advances.sciencemag.org/cgi/content/full/6/19/eaay9466/DC1

View/request a protocol for this paper from *Bio-protocol*.

REFERENCES AND NOTES

1. J. J. Schoenebeck, B. R. Keegan, D. Yelon, Vessel and blood specification override cardiac potential in anterior mesoderm. *Dev. Cell* **13**, 254–267 (2007).
2. M. K. Mateos, D. Barbaric, S.-A. Byatt, R. Sutton, G. M. Marshall, Down syndrome and leukemia: Insights into leukemogenesis and translational targets. *Transl. Pediatr.* **4**, 76–92 (2015).
3. L. M. Piliero, A. N. Sanford, D. M. McDonald-McGinn, E. H. Zackai, K. E. Sullivan, T-cell homeostasis in humans with thymic hypoplasia due to chromosome 22q11.2 deletion syndrome. *Blood* **103**, 1020–1025 (2004).
4. F. Timeus, N. Crescenzio, G. Baldassarre, A. Doria, S. Vallero, L. Foglia, S. Pagliano, C. Rossi, M. C. Silengo, U. Ramenghi, F. Fagioli, L. C. di Montezemolo, G. B. Ferrero, Functional evaluation of circulating hematopoietic progenitors in Noonan syndrome. *Oncol. Rep.* **30**, 553–559 (2013).
5. J. Dudek, C. Maack, Barth syndrome cardiomyopathy. *Cardiovasc. Res.* **113**, 399–410 (2017).
6. B. Van Handel, A. Montel-Hagen, R. Sasidharan, H. Nakano, R. Ferrari, C. J. Boogerd, J. Schredelseker, Y. Wang, S. Hunter, T. Org, J. Zhou, X. Li, M. Pellegrini, J.-N. Chen, S. H. Orkin, S. K. Kurdistani, S. M. Evans, A. Nakano, H. K. A. Mikkola, Scl represses cardiomyogenesis in prospective hemogenic endothelium and endocardium. *Cell* **150**, 590–605 (2012).
7. T. L. Rasmussen, J. Kweon, M. A. Diekmann, F. Belema-Bedada, Q. Song, K. Bowlin, X. Shi, A. Ferdous, T. Li, M. Kyba, J. M. Metzger, N. Koyano-Nakagawa, D. J. Garry, ER71 directs mesodermal fate decisions during embryogenesis. *Development* **138**, 4801–4812 (2011).
8. I. Lyons, L. M. Parsons, L. Hartley, R. Li, J. E. Andrews, L. Robb, R. P. Harvey, Myogenic and morphogenetic defects in the heart tubes of murine embryos lacking the homeo box gene *Nkx2-5*. *Genes Dev.* **9**, 1654–1666 (1995).
9. F. C. Simões, T. Peterkin, R. Patient, Fgf differentially controls cross-antagonism between cardiac and haemangioblast regulators. *Development* **138**, 3235–3245 (2011).
10. A. Caprioli, N. Koyano-Nakagawa, M. Iacovino, X. Shi, A. Ferdous, R. P. Harvey, E. N. Olson, M. Kyba, D. J. Garry, Nkx2-5 represses *Gata1* gene expression and modulates the cellular fate of cardiac progenitors during embryogenesis. *Circulation* **123**, 1633–1641 (2011).
11. Y. L. Schindler, K. M. Garske, J. Wang, B. A. Firulli, A. B. Firulli, K. D. Poss, D. Yelon, Hand2 elevates cardiomyocyte production during zebrafish heart development and regeneration. *Development* **141**, 3112–3122 (2014).
12. A. E. Allen-Jennings, M. G. Hartman, G. J. Kociba, T. Hai, The roles of ATF3 in glucose homeostasis. A transgenic mouse model with liver dysfunction and defects in endocrine pancreas. *J. Biol. Chem.* **276**, 29507–29514 (2001).
13. Y. Okamoto, A. Chaves, J. Chen, R. Kelley, K. Jones, H. G. Weed, K. L. Gardner, L. Gangi, M. Yamaguchi, W. Klomkleaw, T. Nakayama, R. L. Hamlin, C. Carnes, R. Altschuld, J. Bauer, T. Hai, Transgenic mice with cardiac-specific expression of activating transcription factor 3, a stress-inducible gene, have conduction abnormalities and contractile dysfunction. *Am. J. Pathol.* **159**, 639–650 (2001).
14. M. Gilchrist, W. R. Henderson Jr., A. E. Clark, R. M. Simmons, X. Ye, K. D. Smith, A. Aderem, Activating transcription factor 3 is a negative regulator of allergic pulmonary inflammation. *J. Exp. Med.* **205**, 2349–2357 (2008).
15. Z.-Z. Meng, W. Liu, Y. Xia, H.-M. Yin, C.-Y. Zhang, D. Su, L.-F. Yan, A.-H. Gu, Y. Zhou, The pro-inflammatory signalling regulator Stat4 promotes vasculogenesis of great vessels derived from endothelial precursors. *Nat. Commun.* **8**, 14640 (2017).
16. T. Peterkin, A. Gibson, R. Patient, Common genetic control of haemangioblast and cardiac development in zebrafish. *Development* **136**, 1465–1474 (2009).
17. H. Jin, J. Xu, F. Qian, L. Du, C. Y. Tan, Z. Lin, J. Peng, Z. Wen, The 5′ zebrafish scl promoter targets transcription to the brain, spinal cord, and hematopoietic and endothelial progenitors. *Dev. Dyn.* **235**, 60–67 (2006).
18. V. Grajevskaja, J. Balciuniene, D. Balciunas, Chicken β-globin insulators fail to shield the *nkx2.5* promoter from integration site effects in zebrafish. *Mol. Genet. Genomics.* **288**, 717–725 (2013).
19. Y. Kang, C.-R. Chen, J. Massagué, A self-enabling TGFbeta response coupled to stress signaling: Smad engages stress response factor ATF3 for Id1 repression in epithelial cells. *Mol. Cell* **11**, 915–926 (2003).
20. K. L. Targoff, S. Colombo, V. George, T. Schell, S.-H. Kim, L. Solnica-Krezel, D. Yelon, Nkx genes are essential for maintenance of ventricular identity. *Development* **140**, 4203–4213 (2013).
21. A. Ferdous, A. Caprioli, M. Iacovino, C. M. Martin, J. Morris, J. A. Richardson, S. Latif, R. E. Hammer, R. P. Harvey, E. N. Olson, M. Kyba, D. J. Garry, Nkx2-5 transactivates the *Ets-related protein 71* gene and specifies an endothelial/endocardial fate in the developing embryo. *Proc. Natl. Acad. Sci. U.S.A.* **106**, 814–819 (2009).
22. S. L. McKnight, M. D. Lane, S. Gluecksohn-Waelsch, Is CCAAT/enhancer-binding protein a central regulator of energy metabolism? *Genes Dev.* **3**, 2021–2024 (1989).
23. M. Fulco, Y. Cen, P. Zhao, E. P. Hoffman, M. W. McBurney, A. A. Sauve, V. Sartorelli, Glucose restriction inhibits skeletal myoblast differentiation by activating SIRT1 through AMPK-mediated regulation of Nampt. *Dev. Cell* **14**, 661–673 (2008).
24. T. Pavlidou, M. Rosina, C. Fuoco, G. Gerini, C. Gargioli, L. Castagnoli, G. Cesareni, Regulation of myoblast differentiation by metabolic perturbations induced by metformin. *PLOS ONE* **12**, e0182475 (2017).
25. P. Aguiari, S. Leo, B. Zavan, V. Vindigni, A. Rimessi, K. Bianchi, C. Franzin, R. Cortivo, M. Rossato, R. Vettor, G. Abatangelo, T. Pozzan, P. Pinton, R. Rizzuto, High glucose induces adipogenic differentiation of muscle-derived stem cells. *Proc. Natl. Acad. Sci. U.S.A.* **105**, 1226–1231 (2008).
26. E. I. T. Helle, P. Biegley, J. W. Knowles, J. B. Leader, S. Pendergrass, W. Yang, G. R. Reaven, G. M. Shaw, M. Ritchie, J. R. Priest, First trimester plasma glucose values in women without diabetes are associated with risk for congenital heart disease in offspring. *J. Pediatr.* **195**, 275–278 (2017).
27. C.-Y. Zhang, H.-M. Yin, H. Wang, D. Su, Y. Xia, L.-F. Yan, B. Fang, W. Liu, Y.-M. Wang, A.-H. Gu, Y. Zhou, Transforming growth factor-β1 regulates the nascent hematopoietic stem cell niche by promoting gluconeogenesis. *Leukemia* **32**, 479–491 (2018).
28. L. Oburoglu, S. Tardito, V. Fritz, S. C. de Barros, P. Merida, M. Craveiro, J. Mamede, G. Cretenet, C. Mongellaz, X. An, D. Klysz, J. Touhami, M. Boyer-Clavel, J.-L. Battini, V. Dardalhon, V. S. Zimmermann, N. Mohandas, E. Gottlieb, M. Sitbon, S. Kinet, N. Taylor, Glucose and glutamine metabolism regulate human hematopoietic stem cell lineage specification. *Cell Stem Cell* **15**, 169–184 (2014).
29. E. J. Zmuda, L. Qi, M. X. Zhu, R. G. Mirmira, M. R. Montminy, T. Hai, The roles of ATF3, an adaptive-response gene, in high-fat-diet-induced diabetes and pancreatic β-cell dysfunction. *Mol. Endocrinol.* **24**, 1423–1433 (2010).
30. W.-W. Tsai, S. Matsumura, W. Liu, N. G. Phillips, T. Sonntag, E. Hao, S. Lee, T. Hai, M. Montminy, ATF3 mediates inhibitory effects of ethanol on hepatic gluconeogenesis. *Proc. Natl. Acad. Sci. U.S.A.* **112**, 2699–2704 (2015).
31. T. Kaisho, H. Tsutsui, T. Tanaka, T. Tsujimura, K. Takeda, T. Kawai, N. Yoshida, K. Nakanishi, S. Akira, Impairment of natural killer cytotoxic activity and interferon γ production in CCAAT/enhancer binding protein γ-deficient mice. *J. Exp. Med.* **190**, 1573–1582 (1999).
32. G. Zafarana, R. Rottier, F. Grosveld, S. Philipsen, Erythroid overexpression of C/EBPgamma in transgenic mice affects γ-globin expression and fetal liver erythropoiesis. *EMBO J.* **19**, 5856–5863 (2000).
33. M. Alberich-Jordà, B. Wouters, M. Balastik, C. Shapiro-Koss, H. Zhang, A. D. Ruscio, H. S. Radomska, A. K. Ebralidze, G. Amabile, M. Ye, J. Zhang, I. Lowers, R. Avellino, A. Melnick, M. E. Figueroa, P. J. M. Valk, R. Delwel, D. G. Tenen, C/EBPγ deregulation results in differentiation arrest in acute myeloid leukemia. *J. Clin. Invest.* **122**, 4490–4504 (2012).
34. N. D. Wang, M. J. Finegold, A. Bradley, C. N. Ou, S. V. Abdelsayed, M. D. Wilde, L. R. Taylor, D. R. Wilson, G. J. Darlington, Impaired energy homeostasis in C/EBP alpha knockout mice. *Science* **269**, 1108–1112 (1995).
35. S. Liu, C. Croniger, C. Arizmendi, M. Harada-Shiba, J. Ren, V. Poli, R. W. Hanson, J. E. Friedman, Hypoglycemia and impaired hepatic glucose production in mice with a deletion of the C/EBPβ gene. *J. Clin. Invest.* **103**, 207–213 (1999).
36. H. C. Cha, N. R. Oak, S. Kang, T.-A. Tran, S. Kobayashi, S.-H. Chiang, D. G. Tenen, O. A. MacDougald, Phosphorylation of CCAAT/enhancer-binding protein α regulates

GLUT4 expression and glucose transport in adipocytes. *J. Biol. Chem.* **283**, 18002–18011 (2008).

37. E. D. Abel, H. C. Kaulbach, R. Tian, J. C. Hopkins, J. Duffy, T. Doetschman, T. Minnemann, M. E. Boers, E. Hadro, C. Oberste-Berghaus, W. Quist, B. B. Lowell, J. S. Ingwall, B. B. Kahn, Cardiac hypertrophy with preserved contractile function after selective deletion of GLUT4 from the heart. *J. Clin. Invest.* **104**, 1703–1714 (1999).
38. E. L. Gautier, M. Westerterp, N. Bhagwat, S. Cremers, A. Shih, O. Abdel-Wahab, D. Lütjohann, G. J. Randolph, R. L. Levine, A. R. Tall, L. Yvan-Charvet, HDL and Glut1 inhibition reverse a hypermetabolic state in mouse models of myeloproliferative disorders. *J. Exp. Med.* **210**, 339–353 (2013).
39. J. Smith, E. Ladi, M. Mayer-Proschel, M. Noble, Redox state is a central modulator of the balance between self-renewal and differentiation in a dividing glial precursor cell. *Proc. Natl. Acad. Sci. U.S.A.* **97**, 10032–10037 (2000).
40. R. Behringer, M. Gertsenstein, K. Nagy, A. Nagy, *Manipulating the Mouse Embryo: A Laboratory Manual* (Cold Spring Harbor Laboratory Press, ed. 4, 2014).

Acknowledgments

Funding: This work was supported by the National Natural Science Foundation of China (91739108, 81670115, 91839102, and 81870084), the National Science Fund for Outstanding Young Scholars (81722040), the National Key R&D Program of China (2019YFA0801602, 2018YFA0801004, and 2019YFA0802701), the Key-Area Research and Development Program of Guangdong Province (2019B020227001), and the Key Research Program of Frontier Sciences, CAS (QYZDB-SSW-SMC034). We thank LetPub for linguistic assistance. **Author contributions:** H.-M.Y., L.-F.Y., Q.L., Z.P., C.-Y.Z., Y.X., and D.S. performed experiments and analyzed data. A.-H.G. and Y.Z. designed the research plan and wrote the paper. **Competing interests:** The authors declare that they have no competing interests. **Data and materials availability:** ChIP-sequencing data have been deposited in ArrayExpress with the accession number E-MTAB-6575. All data needed to evaluate the conclusions in the paper are present in the paper and/or the Supplementary Materials. Additional data related to this paper may be requested from the authors.

Submitted 3 August 2019
Accepted 27 January 2020
Published 6 May 2020
10.1126/sciadv.aay9466

Citation: H.-M. Yin, L.-F. Yan, Q. Liu, Z. Peng, C.-Y. Zhang, Y. Xia, D. Su, A.-H. Gu, Y. Zhou, Activating transcription factor 3 coordinates differentiation of cardiac and hematopoietic progenitors by regulating glucose metabolism. *Sci. Adv.* **6**, eaay9466 (2020).

Science Advances

Activating transcription factor 3 coordinates differentiation of cardiac and hematopoietic progenitors by regulating glucose metabolism

Hui-Min Yin, Li-Feng Yan, Qian Liu, Zheng Peng, Chi-Yuan Zhang, Yu Xia, Dan Su, Ai-Hua Gu and Yong Zhou

Sci Adv **6** (19), eaay9466.
DOI: 10.1126/sciadv.aay9466

Science Advances (ISSN 2375-2548) is published by the American Association for the Advancement of Science, 1200 New York Avenue NW, Washington, DC 20005. The title *Science Advances* is a registered trademark of AAAS.